Final Report

Federal Agency:
United States Geological Survey
Volcanic Science Center
345 Middlefield Road
Menlo Park, CA 94025

Recipient Organization:
Array Information Technology
2020 Cedar Street
Berkeley, CA 94709

Contract Number:
GS-35F-0023P

Project Title:
Analysis of Seismic Data in the Clear Lake Volcanic Field

Project Period:
06/01/2016 – 05/31/2017

Principal Investigator:
Dr. Roland Gritto
Senior Geophysicist
roland.gritto@arrayinfotech.com
510-704-1848
Co-Principal Investigator:
Avinash Nayak
Berkeley Seismological Laboratory
avinash@seismo.berkeley.edu

Date:
May 31, 2017

USGS Project Team:
Dr. Margaret Mangan
Dr. David Shelly

1 Overall Project Objective

The goal of this scoping study includes the analyses of seismic data in the Clear Lake/Geysers region to search for evidence and possibly the location of the heat source that is sustaining the Clear Lake/Geysers geothermal system. It was originally planned to utilize broadband data continuously recorded in Clear Lake/Geysers area over a period of approximately 12 months from 2012 to 2013. These data were supposed to be supplemented by data from the Berkeley Digital Seismic Network (BDSN) and from the Northern California Seismic Network (NCSN). However, to improve spatial extent and resolution in the region of interest, it was decided to add waveform data from other permanent stations and temporary network campaigns that have been conducted in recent years. The final goal of the scoping study is to provide recommendations on the most promising survey sites for future MT and seismic campaigns in support of the USGS CalVO.

2 Work Scope

2.1 Seismic Networks

The continuous seismic stations, for which data were investigated for the analyses of teleseismic waves and noise cross-correlations, are presented in Figures 1 and 2. The seismic stations include broadband stations deployed by Roland Gritto (Array IT) in collaboration with GFZ Potsdam (The Geysers Broadband Network, GBN), broadband stations of NCSN (Northern California Seismic Network), BDSN (Berkeley Digital Seismic Network) and broadband stations deployed during the Mendocino Experiment (EarthScope Flex array FAME). A wide variety of short period (1 Hz, 2 Hz, 4.5 Hz, 8.0 Hz) sensors and accelerometers available in the region was also included. It is hoped that the capabilities of these high frequency/low gain sensors evaluated in this study will lead to full utilization of the spatially very dense NCSN and BDSN throughout Northern California.

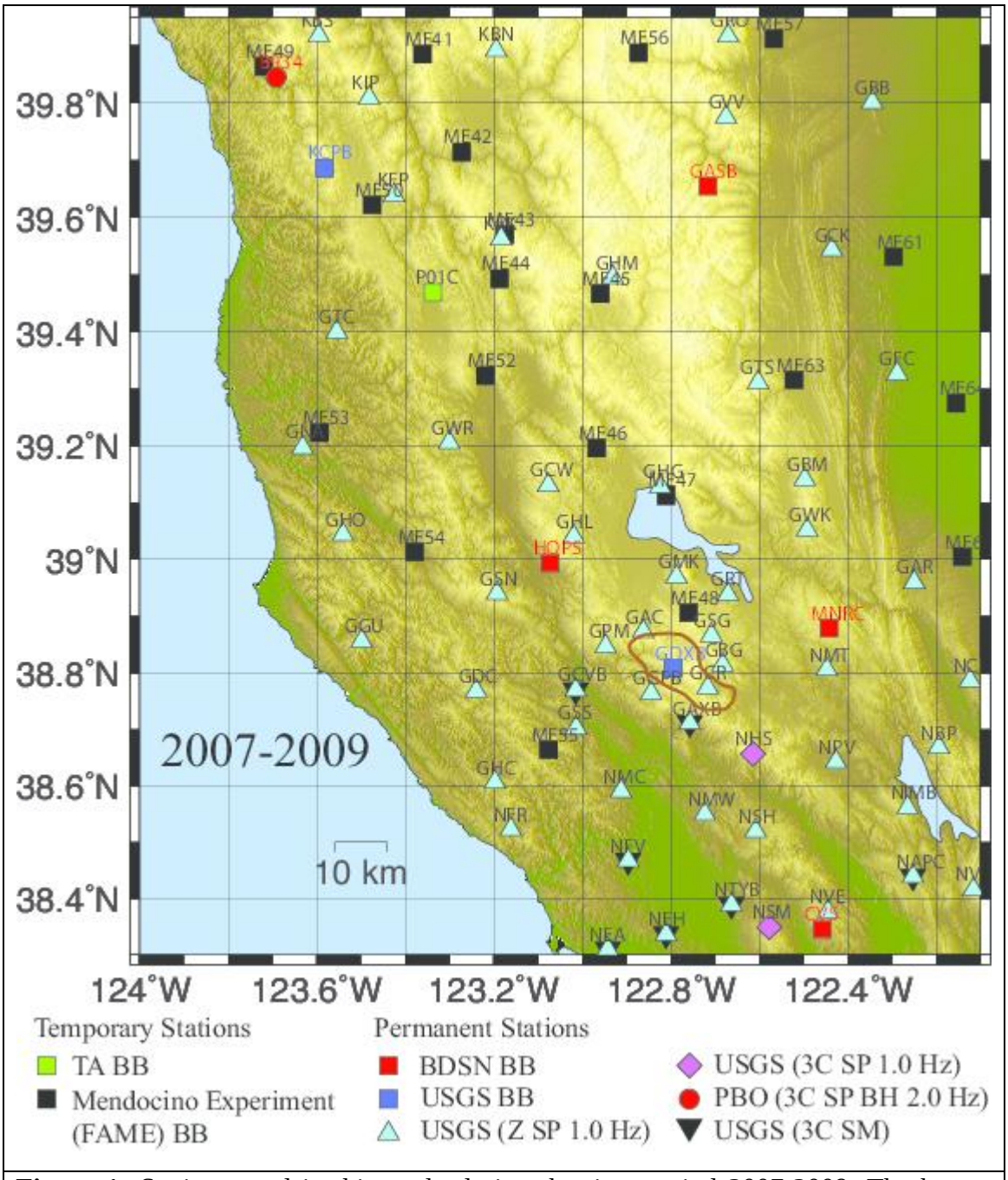

Figure 1: Stations used in this study during the time period 2007-2009. The brown polygon is the outline of The Geysers geothermal field.

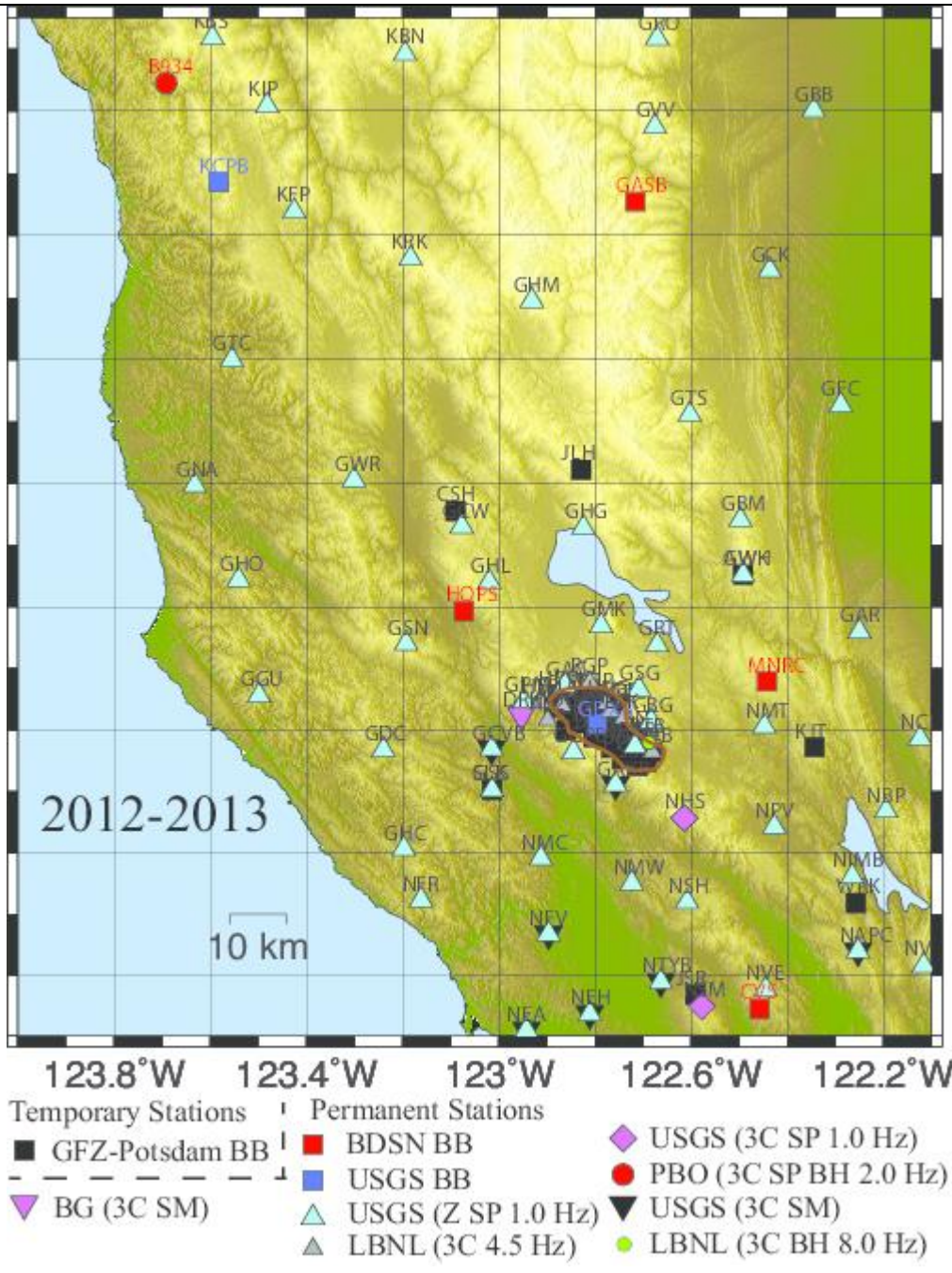

Figure 2: Stations used in this study during the time period 2012-2013. The brown polygon is the outline of The Geysers geothermal field.

2.2 Analysis of Teleseismic Waves

After analyzing the teleseismic waveform data, it was concluded that for the objectives of the present scoping study teleseismic P-wave travel time residuals provide more reliable estimates and better spatial coverage of low velocity anomalies in the crust below the stations than the analysis of teleseismic S-waves. While long period S-waves from teleseismic events offer poor resolution, receiver function studies that could have mitigated the lack of resolution are not feasible, because there are very few 3-component seismic stations close to Clear Lake. Therefore, P-wave travel time residuals were analyzed utilizing a technique that eliminates source dislocations and effects of inhomogeneities outside the common paths as discussed below.

Teleseismic P-wave travel time residuals were analyzed for 21 $M \geq 7$ earthquakes recorded by most of the seismic stations displayed in Figure 3. For each earthquake, relative delay times were defined as: [observed arrival time – mean(observed arrival time)] – [predicted arrival time – mean(predicted arrival time)]. The observed arrival times were calculated from waveform cross correlation of P-waves filtered at 0.8-2.0 Hz using the software AIMBAT (VanDecar & Crosson, 1990; Lou et al., 2013). The removal of the mean event residual reduces travel time anomalies resulting from incorrect hypocenter location, origin time, and inhomogeneities in structure along ray paths outside the common region. The waveforms at some stations to the southwest of Clear Lake and in the northwestern part of The Geysers were very dissimilar to waveforms recorded at nearby stations (Figure 6) necessitating manual picking of arrival times at these stations (e.g., GSG, ME48, and GBM for some events). This agrees with a previous teleseismic travel-time study that also noted severe waveform changes and emergent arrivals near Mt. Hannah and The Geysers (Oppenheimer & Herkenhoff, 1981). The maps in Figures 4 and 5 display preliminary results of teleseismic travel time residuals in The Geysers – Clear Lake region. Blue and red squares denote, respectively, mean values of fast and slow travel time residuals relative to the reference model AK135 (Kennett et al., 1995), while the size of the symbols is proportional to the amplitude of the travel time residual. The residuals are corrected for clock/time-stamp errors (discussed in the following section) and elevation using a reduction velocity of ~ 4 km/s. Our preliminary results denote negative residuals in the northwest Geysers extending towards the southern part of Clear Lake. The extension towards Clear Lake trends towards the most recent volcanism including Mt. Konocti and Mt. Hana to the south. Our preliminary results agree with those by Gritto et al. (2013), who conducted a local 3D tomography study for V_P and V_S and with those of Oppenheimer and Herkenhoff (1981). The prominent velocity contrast between the northwest and southeast sections of The Geysers is also observed in the local earthquake tomography study (depths < 4.5 km). While Oppenheimer and Herkenhoff (1981) and Benz et al. (1992) showed that the low velocity anomaly south of Clear Lake extends to ~30 km depth, decreasing from ~ –10% to –15% at ~15 km to ~ –4% at ~30 km, body wave tomography and short-period noise cross-correlation waveform-modeling studies indicate shallow low velocities to the northeast of The Geysers, which can be attributed to rocks of the Clear Lake volcanics and interbedded sedimentary deposits of the Great Valley sequence (Hearn et al. 1981; Eberhart-Phillips 1986; Julian et al. 1996; Nayak et al. 2017). Eberhart-Phillips and Oppenheimer (1984) also estimated a 0.25 s P-wave station correction at GSG with respect to GBG, which must be a result of very shallow low velocities. In other studies,

Stanley et al. (1998) attribute shallow (up to ~5 km) low velocities near Mt. Hannah region to Mesozoic argillates. Their local earthquake P-wave tomography results indicate a low-resolution low-velocity anomaly at depths ~8-12 km extending eastwards from below The Geysers-Clear Lake region. The latest local earthquake P-wave tomography results (Thurber et al., 2009) indicate low velocities only up to ~–5% at depths ~8-14 km below The Geysers-Clear Lake region. A joint inversion of local and teleseismic earthquake body-wave travel times may be necessary to resolve the velocities at shallow and lower crustal depths.

Extraction of relative travel time residuals for ~100 earthquakes is expected to be sufficient for performing teleseismic P-wave tomography. An example of the dissimilarity between stations to the southwest of Clear Lake can be seen in Figure 6, which reveals that higher frequencies in the waveform at station ME48 appear to be strongly attenuated compared to other nearby stations.

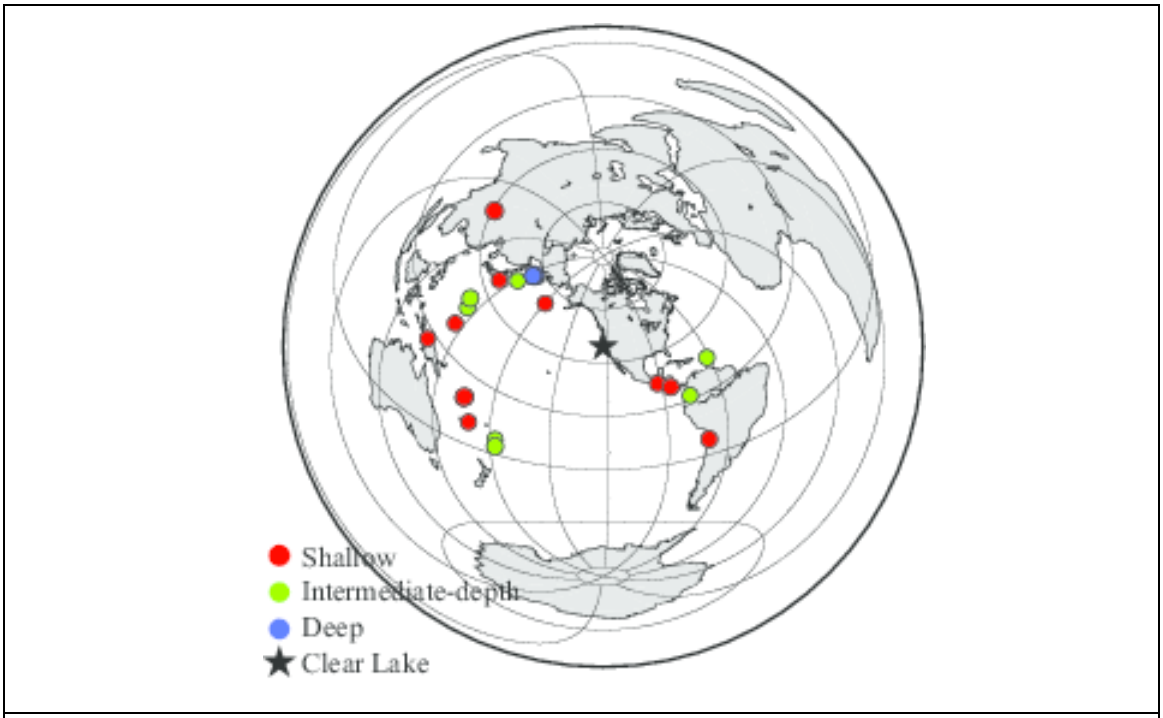

Figure 3: Epicenters of earthquakes at teleseismic distances analyzed thus far in this study.

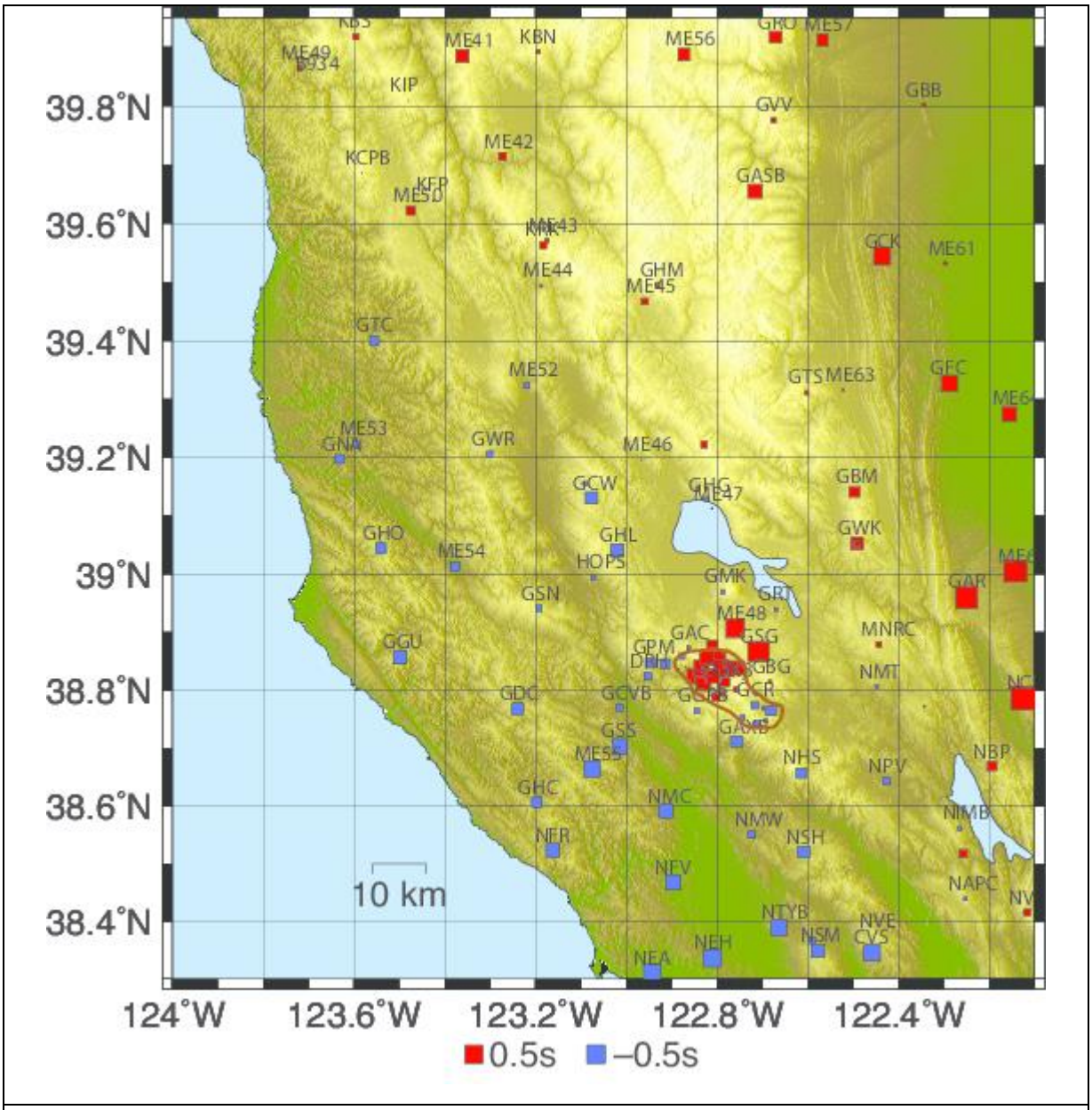

Figure 4: Map of relative travel-time residuals (explanation of symbols in the text). The key below the map provides a measure of absolute value of the residuals.

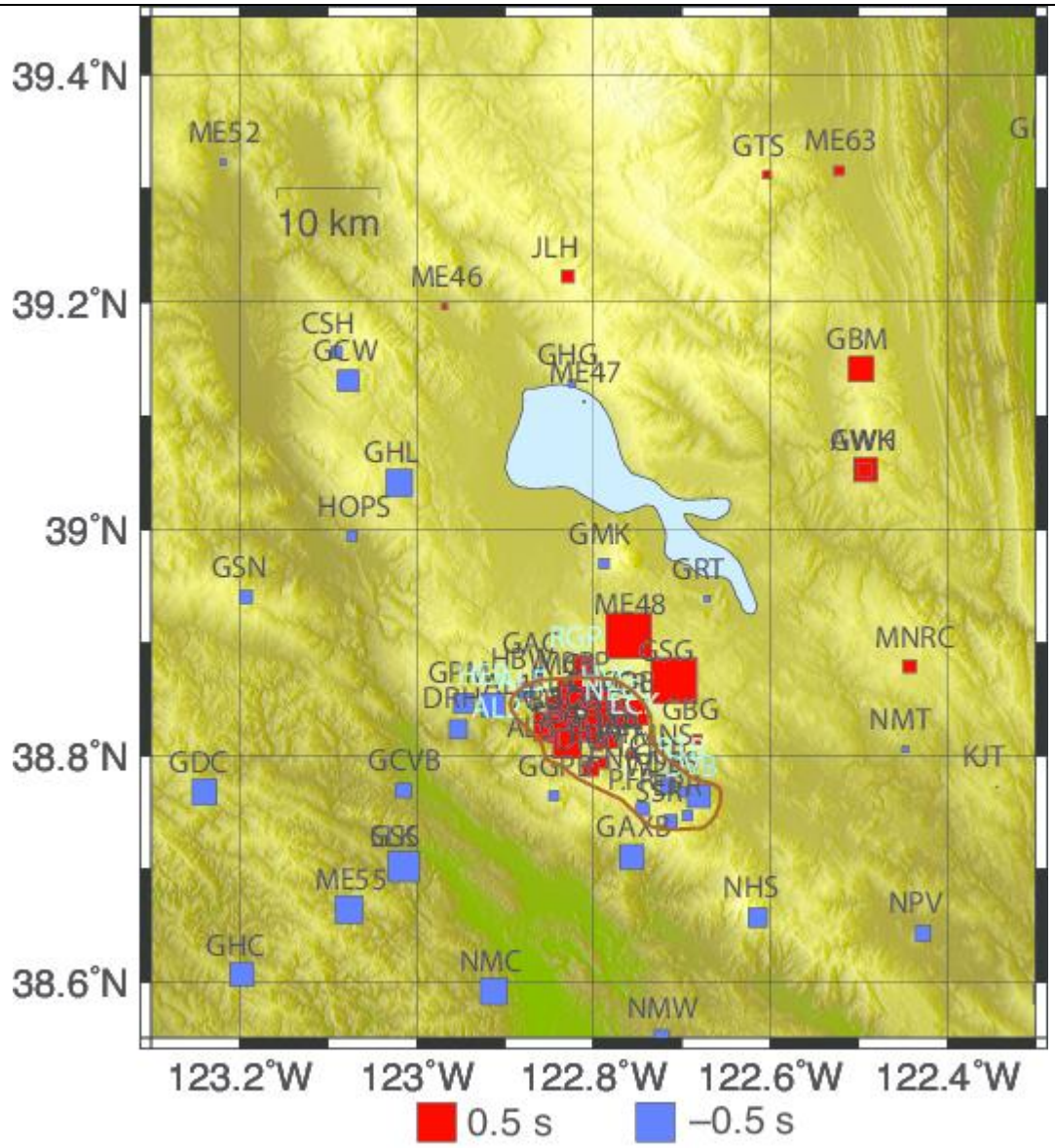

Figure 5: Expanded map of relative travel-time residuals (explanation of symbols in the text) in the area around Clear Lake. The key below the map provides a measure of absolute value of the residuals.

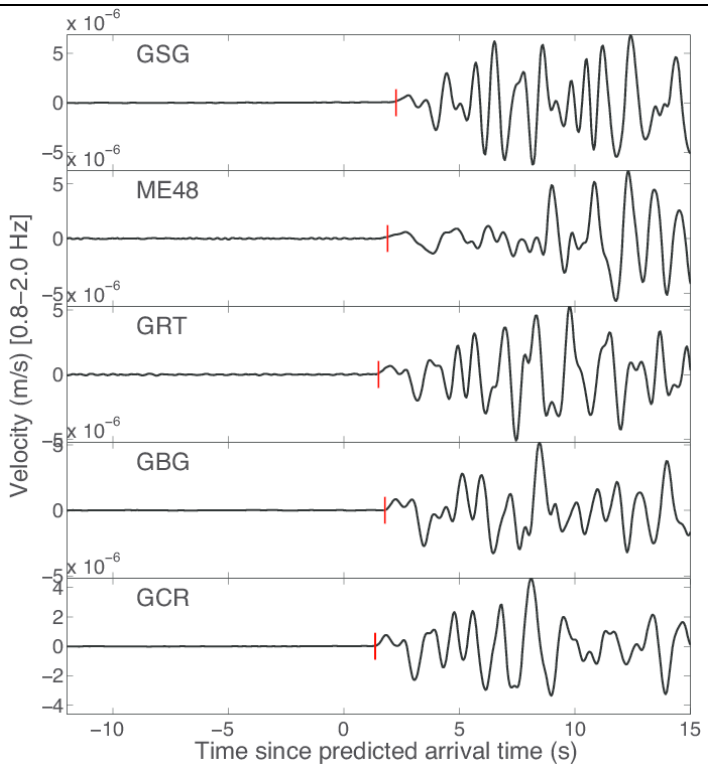

Figure 6: P-waves of a teleseismic earthquake recorded at stations southwest of Clear Lake. Higher frequencies in the waveform at station ME48 appear to be strongly attenuated compared to other nearby stations.

2.3 Long Period Earthquakes and Tremors

Long Period Earthquakes

Deep Long-Period (LP) volcanic earthquakes are often associated with migration of magma in the Earth's crust and have been used as precursors to volcanic eruptions (Chouet, 1996). LP events have also been observed at mid-crustal depth below Clear Lake and represent the best seismological evidence to date for magmatic movement associated with the Clear Lake volcanic system (Pitt et al., 2002). In contrast to the more common brittle failure-type earthquakes, LP events are devoid of high frequency (> 5 Hz) energy and show distinct spectral peaks in a narrow pass band (~1-5 Hz). As reported by Pitt et al. (2002), clusters of LP events have been detected below the southwestern lakeshore at depths between 12 km and 27 km and about 5 km to the northeast of Clear Lake at a focal depth of ~ 18 km. All LP events occur at depths below the seismogenic transition zone as defined by the maximum depth of the brittle failure-type events. Interpretations of LP events include the resonance of fluid-filled cracks (Chouet, 1992) and nonlinear fluid flow along conduits with irregular geometry (Julian, 1994), which may suggest evidence for a volcanic system evolving towards eruption (Pitt et al., 2002).

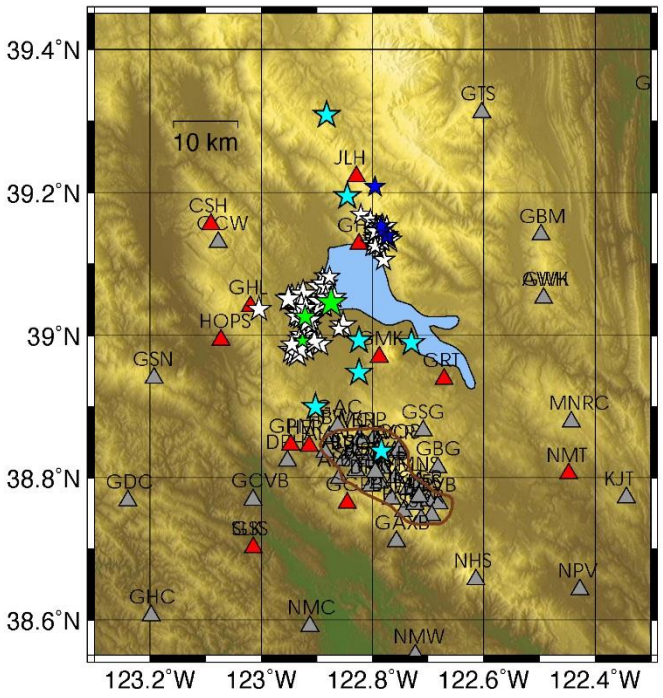

Figure 7: Locations of LP and seismic tremor events. LP events (white, blue and green stars) are from the 1987 to 2016 NCSS catalog, while blue and green stars denote events whose origin times coincide with the GBN and FAME deployments, respectively. Seismic tremor locations are denoted by cyan stars. Triangles represent station locations with red triangles indicating those used for detecting the tremor. Clear Lake is represented by the blue body of water, while The Geysers steam field is denoted by the outline of the brown polygon.

The white, blue and green stars in Figure 7 denote epicentral locations of LP events recorded in the NCSS catalog from 1987-2016. Blue and green stars denote events with origin times that coincide with the GBN and FAME deployment, respectively. It is interesting that the LP events cluster in two locations, one to the north of Clear Lake and the other to the west. Given location accuracies the observed gap of ~ 10 km is likely to be real. We have examined waveform data from GBN and the USGS NC network for LP events identified in the NCSS catalog. Figure 8 compares the waveforms at several stations for an Md 1.4 event identified as a deep LP event in the NCSS catalog. The event occurred on July 3, 2013 at 00:13:37.88 UTC, 39.15317, -122.78433 at a depth of 16.1km. The arrival times at the stations indicate that this LP event is located near stations GHG and JHL. The dominant energy is between 1 to 10 Hz. Figure 9 shows the waveforms for an Md 1.5 LP event at station CSH. Clear P and S waves are identifiable. Assuming a Brune stress drop of 1 MPa the corner frequency is expected to be approximately 33 Hz. We have fit synthetic spectra to the vertical component record, assuming a layered elastic model and regional values for Q, and found the corner frequency to be approximately 5 Hz. This corner frequency

implies a 0.003 MPa (3 kPa) stress drop. This stress drop estimate is of the order inferred from triggered tremor that occur at this depth elsewhere on the San Andreas fault (e.g., Thomas et al., 2009). Thomas et al. (2016) investigated the spectra of Low Frequency Earthquakes (LFE) thought to be the basis of NVT (Shelly et al., 2006) and found that they have corner frequencies consistent with stress drops on the order of 10 KPa implying slow (20% of the shear wave velocity) rupture speed, and locally high fluid pressure. Thus, the LP events at Clear Lake appear to have characteristics similar to LFE on the San Andreas fault. In Thomas et al. (2016) repeating LFE are utilized for spectral analysis correcting for path effects, however, at Clear Lake it is presently unknown whether the LP events may be repeating.

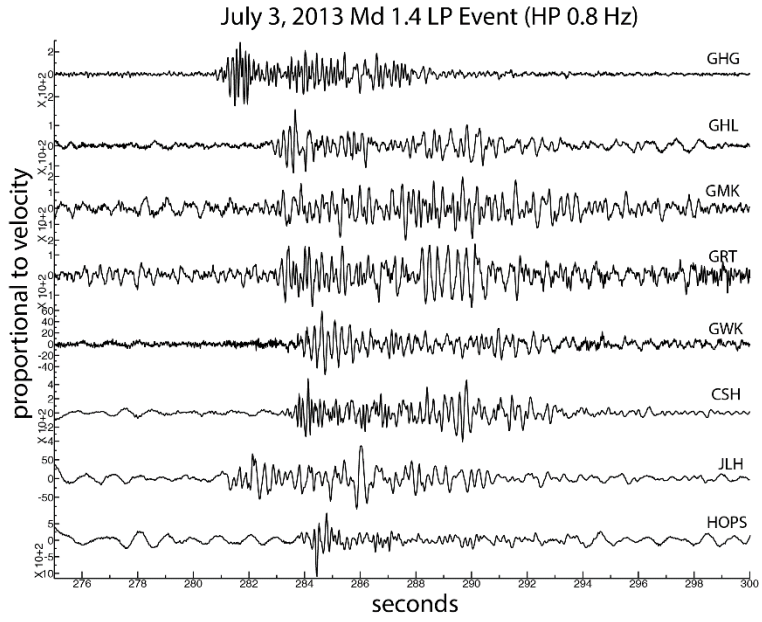

Figure 8: Examples of vertical component records for an LP event. Stations beginning with a "G" are 1 Hz geophones recording only the vertical component. Stations CSH, JLH and HOPS are broadband. This particular LP event is located near GHG and JLH and is from the northern cluster of LP events.

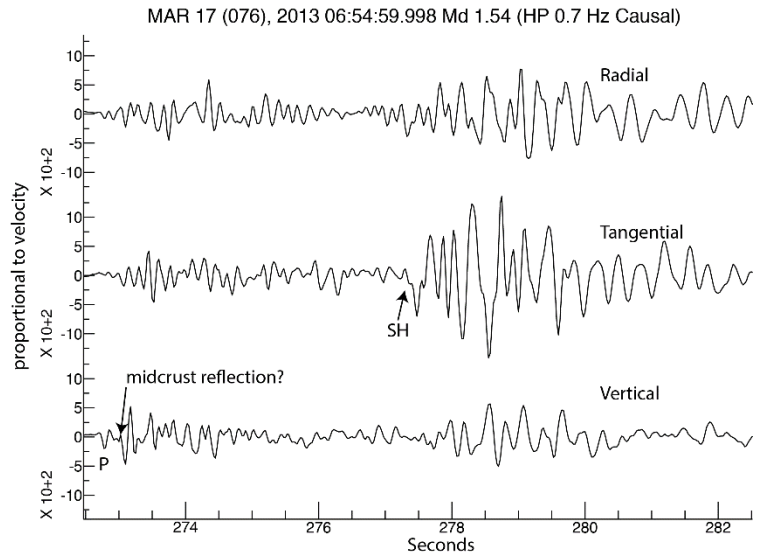

Figure 9: Three component velocity record of an Md 1.5 LP event on March 17, 2013.

Seismic Tremor

Seismic Tremor (seismic sources generating long-duration, low-amplitude seismic signals, generally in the 2-8 Hz band, lasting several minutes or more with no clear P or S arrivals) have been found in both shallow volcanic and much deeper non-volcanic environments with semi-brittle to ductile rheologies (Schwartz and Rokosky, 2007). Fluids are believed to play an important role in their generation and they are particularly responsive (sensitive) to deformation and very small changes in shear-stress (e.g., Rogers and Dragert, 2003; Aguiar et al., 2009; Thomas et al., 2009; Nadeau and Guilhem, 2009; Guilhem et al., 2010). Their strong sensitivity to shear- and relative insensitivity to normal-stress changes also indicate that they occur in high pore-fluid pressure environments (Shelly et al., 2006; Song et al., 2009; Thomas et al., 2009; Nadeau and Guilhem, 2009).

Using envelope median filtering and cross-correlation methods, preliminary 24-hour searches for seismic tremor on 20 arbitrarily chosen days was carried out in the proposed study area using data from four seismic network stations (NC, BK, BG and GBN). The search identified a number of tremor events. A subset of eight of these events were located using a grid-search and simple half-space velocity model (Figures 7 and 10). The events occurred primarily between The Geysers steam field (to the south) and Clear Lake, (to the north), though two of the eight preliminary locations occurred north of Clear Lake, suggesting more than one source region for tremor in the area. Depths of the tremor ranged between 10 to 35 km.

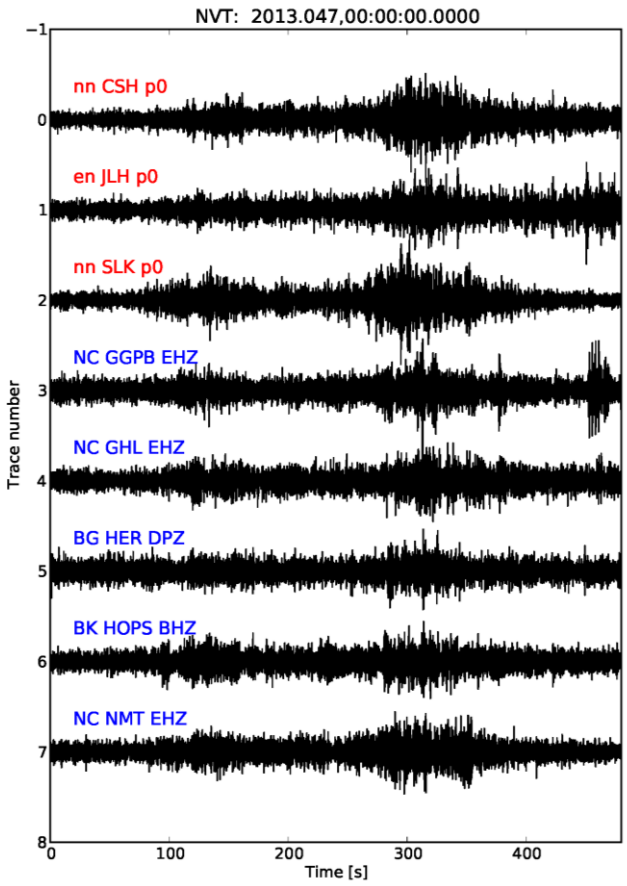

Figure 10: Waveforms of the 2013.047 NVT event band-pass filtered 3-8 Hz recorded on stations from four seismic networks in The Geysers area. Stations from permanent networks (NC, BK, and BG) are labeled in blue, while stations from the GBN deployment are labeled in red.

2.4 Derivation of Empirical Green Functions from Ambient Noise Cross Correlation

We cross-correlated and stacked ambient noise recorded at all components of all stations shown on the maps in Figures 1 and 2 during time periods ~2005-2009 and ~2012-2016 following methodologies of Bensen et al. (2007), Seats et al. (2012) and Lin et al. (2014). For temporal normalization, the daily waveforms were filtered in two different passbands ~ 0.025 Hz to 0.1 Hz, and 0.1 to 1.0 Hz. For each filtered trace, a smoothed envelope was constructed with the absolute value of the filtered trace by replacing each sample with the maximum value of the samples around it in a window followed by multiplication with a cosine taper. The duration of the window and width of the cosine taper are a function of the frequency passband of the filter. A reciprocal weighting factor was estimated for sections of the smoothed envelope where the amplitude exceeded a certain threshold. The threshold is a scaled daily room-mean-squared average of the

smoothed envelope. The minimum weighting factors from all passbands and components were selected for a particular station and applied to the original waveforms. For spectral normalization and cross-correlation, 30 minute long windows overlapping at 75% were selected and the spectrum of each component at a station was normalized by the smoothed mean amplitude spectrum of all components for that station. Cross-correlations of all windows were stacked to get daily cross-correlations and all daily correlations for each station pair were stacked to obtain a final cross-correlation after correcting for clock errors (see the following section). The cross-correlations in the EW-NS-Z reference frame were rotated to the T-R-Z reference frame (T=tangential, R=radial, Z=vertical). Fundamental mode Rayleigh wave phase velocities were measured at different time periods between 1.5 s and 10 s on ZZ, ZR and RZ components of the noise cross-correlations (1st letter: force direction, 2nd letter: displacement direction). It was not possible to use the better quality Love waves on the TT components, because the distribution of 3-component stations in our study region is non-uniform and most stations have vertical component sensors only. Therefore, measurement of Love wave dispersion curves was not pursued. The low-gain accelerometers collocated with some of the vertical component sensors of NCSN (e.g., NEH, NTYB, etc.) returned usable noise-correlations only up to a distances of ~40 km. Excellent cross-correlations were retrieved for pairs of broadband sensors and vertical component 1.0 Hz sensors up to distances of ~100 km. These short-period sensors form the backbone of NCSN and could significantly improve resolution of future crustal surface-wave tomography studies over previous ambient noise surface-wave tomography studies that have used much sparser networks of broadband stations (e.g., Porritt et al., 2011). We also attempted the C^3 method (Stehly et al. 2008; Spica et al., 2016) to retrieve cross-correlations between the two asynchronous temporary broadband networks – GBN and FAME using the BDSN and NCSN short-period and broadband stations as permanent reference stations. We could reconstruct usable surface waves for pairs with only two stations of the FAME network – ME52 and ME53. Figure 11 shows ZZ component waveforms binned by interstation distance.

The dispersion curves were measured with the Automatic Frequency-Time Analysis (AFTAN) code (Bensen et al., 2007). For interstation distances from 10 km to 220 km, the unit-less width factor of the Gaussian window was made distance-dependent (from 12 to 100) and selected based on tests on Rayleigh wave synthetics computed using the modal summation method (Herrmann, 2013) and the GIL7 velocity model for the California Central Coast Ranges (Stidham et al., 1999). The reference dispersion curve required for measurement of phase velocity along each path was constructed using the latest USGS 3D velocity model (v 8.3.0) for northern California (Brocher 2008; Aagaard et al., 2010). We divided each path into ~2-10 km long segments. For each segment, we extracted a 1D velocity profile from the 3D model and computed synthetic Rayleigh wave dispersion curve using the method by Herrmann (2013). A composite dispersion curve was estimated for each path from the total phase travel-time. The longest period measured for each path was limited by the criteria: distance $R \geq 1.8\lambda$, where λ is Rayleigh-wave wavelength as a function of period T. This threshold is less conservative than what is commonly used in other studies ($\sim R \geq 3.0\lambda$). The distribution of interstation distances in our small study region peaks at ~60 km. Therefore, the criteria was relaxed to include more long-period measurements at the cost of greater errors in the measurements. A frequency-dependent signal-to-noise (SNR) ratio

was defined as the ratio of the peak signal amplitude in the surface-wave window to the peak amplitude at any prior time. The SNR thresholds ranged between 2.5 for shorter periods and 1.8 for the longest periods. We were able to obtain sufficient phase velocity measurements between periods ~1.7 s and ~6.0 s for Rayleigh wave tomography. However, insufficient measurements were obtained at shorter periods, while the inversions results at longer periods returned large residuals indicating large errors in the measurements. Figure 12 shows Rayleigh wave dispersion measurements from our noise cross-correlation analysis.

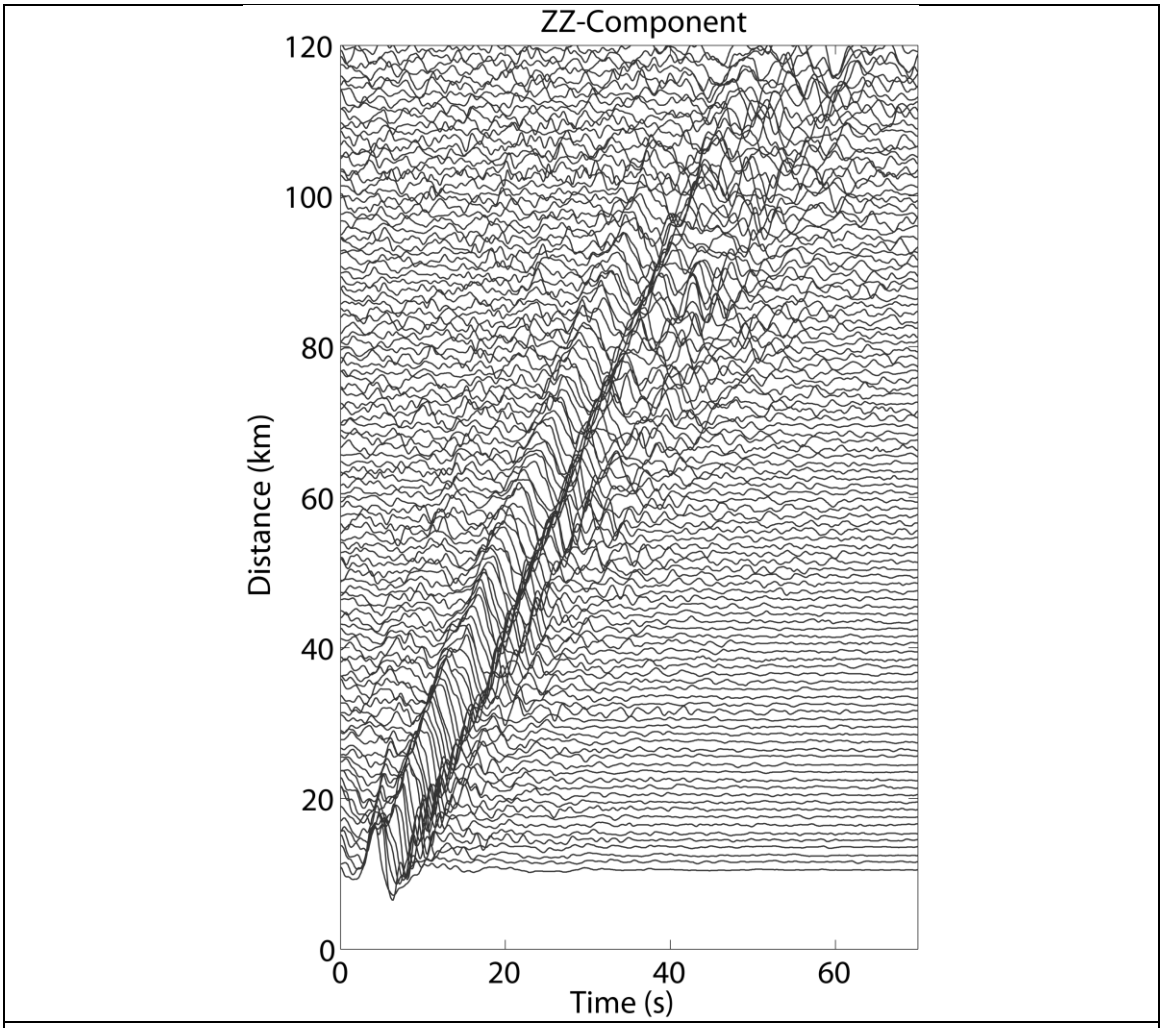

Figure 11: ZZ component noise cross-correlations. Each trace is an average of multiple noise cross-correlations stacked in 1.0 km interstation distance bins.

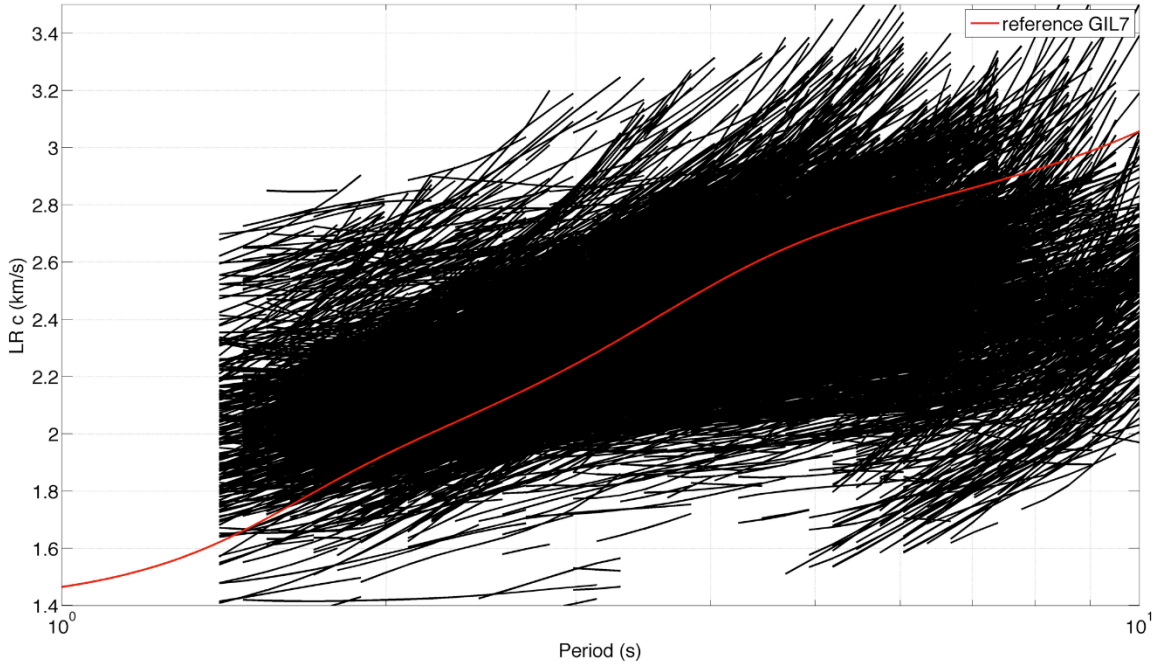

Figure 12: Rayleigh wave phase velocity dispersion measurements from ZZ, ZR and RZ component noise cross-correlations. The red line represents the dispersion curve derived from the GIL7 velocity model.

Clock/Time-Stamp Errors

The comparison of noise cross-correlations computed over 24-hour windows with a reference noise cross-correlation trace stacked over a long time period (> 1 year) can be used to detect clock or time-stamp errors (Sens-Schönfelder, 2008). We detected time-stamp errors in data downloaded from NCEDC (Northern California Earthquake Data Center) for multiple NCSN stations. An example is shown in Figure 13. Some of the larger errors at NC stations incldue KBS (~1 s for ~11 days), GDXB (~4 s for ~25 days), NHS (~1 s for ~58 days, ~5 s for ~100 days) and NSM (~1 s for ~145 days). All teleseismic P-wave arrival times and noise cross-correlations in this study were subsequently corrected for the detected errors.

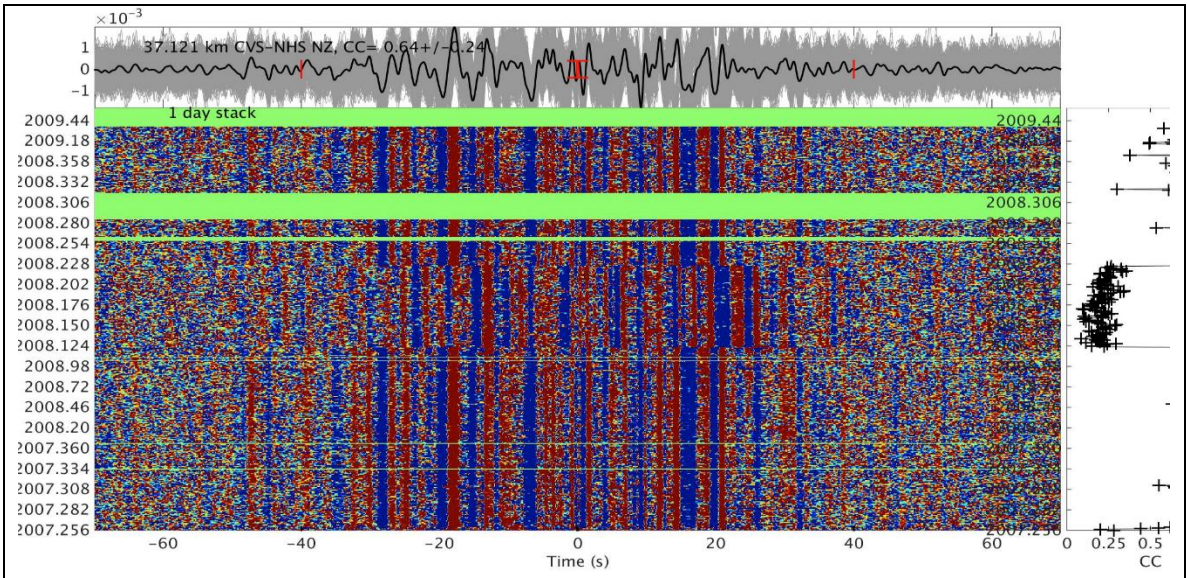

Figure 13: The top trace shows daily NZ component noise cross-correlations (gray traces) between stations BK-CVS and NC-NHS from ~2007 to ~2008. The black waveform is the reference stack. Plot at bottom left shows the daily noise cross-correlations through time. A 5-second shift can be clearly seen between ~2008.123 and ~2008.225 corresponding to the decrease in correlation between daily noise cross-correlations and the reference stack in the bottom right plot.

2.5 Surface Wave Tomography

Methodology

The Rayleigh wave dispersion measurements described in the section 2.4 were inverted to generate Rayleigh wave phase velocity maps at discrete periods from ~1.7 s to ~6.0 s, using the Fast Marching Surface-wave Tomography (FMST v1.1) package by Rawlinson (2008). The forward modeling of travel-times in FMST is based on the fast marching method, which solves the Eikonal equation numerically using a finite-difference scheme and tracks advancing wavefronts on a 2D spherical grid appropriate for surface wave propagation (Rawlinson and Sambridge, 2004). Unlike other popular surface wave tomography codes that assume straight rays between the source and the receiver (e.g., tomo_sp_cu v.1.1, Barmin et al., 2001), the fast marching method accounts for ray bending in arbitrarily complex media, which is appropriate for our small study region (Rawlinson and Sambridge, 2004). Our node spacing was 0.1° in an area 38.2°N to 40.1°N and -123.9°E to -121.8°E resulting in 20 by 22 model parameters at each period. For all periods, a constant velocity field was assumed for the initial 2D phase velocity map with the velocity equal to the mean of all phase velocity measurements for that period and an assumed model covariance ~0.3 km/s (subsequently used in the inversion). The fast marching method interpolates this grid on a smooth continuous velocity grid using cubic B-spline patches and calculates the synthetic phase

travel-times and Fréchet derivatives. A subspace inversion routine performs a linear inversion of the residuals between observed and modeled travel-times using the Fréchet derivatives to calculate the model perturbations. Iteratively, the velocity model is updated following the recalculation of the raypaths, model travel-times and Fréchet derivatives until the misfit between the observed and modeled phase travel-times decreases to a stable value (< 10 iterations). The inversion uses damping and smoothing parameters to arrive at a stable and smooth model. A range of damping and smoothing parameters from (1, 2, 4, 10, 50, 125) and (1, 4, 10, 20, 40 and 100), respectively, was tested. The model features shown in the phase velocity maps in the *Results* section are generally stable with respect to the choice of damping and smoothing parameters in and around areas with good raypath coverage. After a preliminary inversion with strong smoothing and damping, measurements with residuals > 5 s were removed as part of a data cleaning procedure (e.g. Barmin et al., 2001; Lin et al., 2008). The quantity of removed data ranged from ~0% at shortest period to ~10% at the longest period. We subsequently repeated the inversions with the cleaned-up measurements. At all periods, the root-mean-square (RMS) value of residuals decreased from the initial to the final model indicating a successful inversion. The final RMS values range from ~0.8 s at ~1.6 s to ~1.6 s at ~6.0 s periods, which are greater than values achieved by other regional studies (~1.0 s for western United States regional tomography, Lin *et al.* 2008). This is likely due to our less conservative distance-period criteria ($R \geq 1.8\lambda$).

Results

The following tomography results present a series of phase velocity maps at discrete periods. Each figure is comprised of two subplots. The left plot presents the phase velocity map with node positions and major fault traces. The period (T), maximum depth sensitivity (d=0.63λ; Xia et al., 1999), number of measurements (N), damping (e) and smoothing (n) parameters and the final RMS residual (res) are indicated at the left side of each subplot. The right subplot, in addition, shows the raypaths and the station distribution. It is noted that the color bars on the phase velocity maps are individually scaled such that direct comparison of anomalies between maps should be done with caution.

Figure 14 shows the phase velocity map for the period T=1.63s. This period has the maximum sensitivity around 2.3 km depth. Even though the number of phase measurements is smallest at this period (N=503), some features are consistent with longer periods as will be pointed out below. The low velocity anomaly along the trace of Highway 101 in the Santa Rosa Valley is indicative of shallow alluvial deposits. This feature is prominent throughout the following phase velocity maps exhibiting lower velocities than the surrounding region. This is consistent with findings by Eberhart-Phillips (1986), who reported low velocities to at least 6 km depth along the Maacama and Healdsburg-Rodgers Creek (HRC) fault zones. The low-velocity region was widest at the en-echelon junction of the Maacama and HRC fault zones (Eberhart-Phillips, 1986). Additionally, a low velocity anomaly is observed between The Geysers and Clear Lake that appears to be separating into a northern and southern feature as will be seen on the following phase velocity maps. A curious feature is the velocity high below the southeastern part of Clear Lake,

which might be a manifestation of shallow lava flows from previous eruptions of Mt. Konocti. However, this feature should not be overinterpreted as the resolution of the estimates at T=1.63s is low as can be seen by the paucity of raypaths outside The Geysers reservoir (Figure 14, right panel).

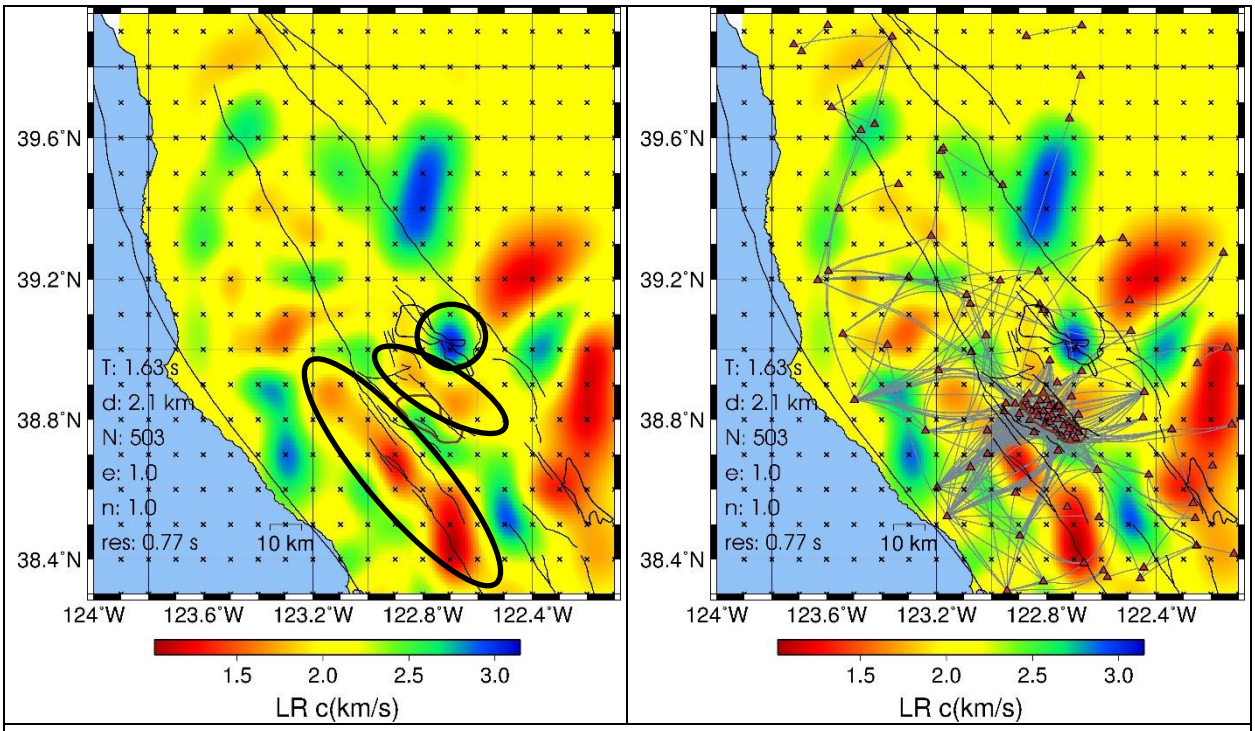

Figure 14: Rayleigh wave phase velocity maps for a period of T=1.63 s for the region surrounding The Geysers/Clear Lake volcanic complex. **left:** phase velocity map. **right:** phase velocity map with raypaths (gray lines) between seismic stations (red triangles). T: Period of inverted phase velocity; d: depth of the maximum sensitivity; N: number of phase velocity measurements; e: damping; n: smoothing; res: time residual. Small crosses denote nodes used in the inversion. Node spacing is ~ 10 km.

The phase velocity map of the next period at T=1.80s is displayed in Figure 15. The number of phase measurements that are the basis for this map is 50% higher than in Figure 14, which provides better resolution for the latter. However, due the different color scale the anomalies are suppressed in amplitude. Therefore, the only feature to be pointed out is the before-mentioned low-velocity region that coincides with the en-echelon junction of the Maacama and Healdsburg-Rodgers Creek (HRC) fault zones.

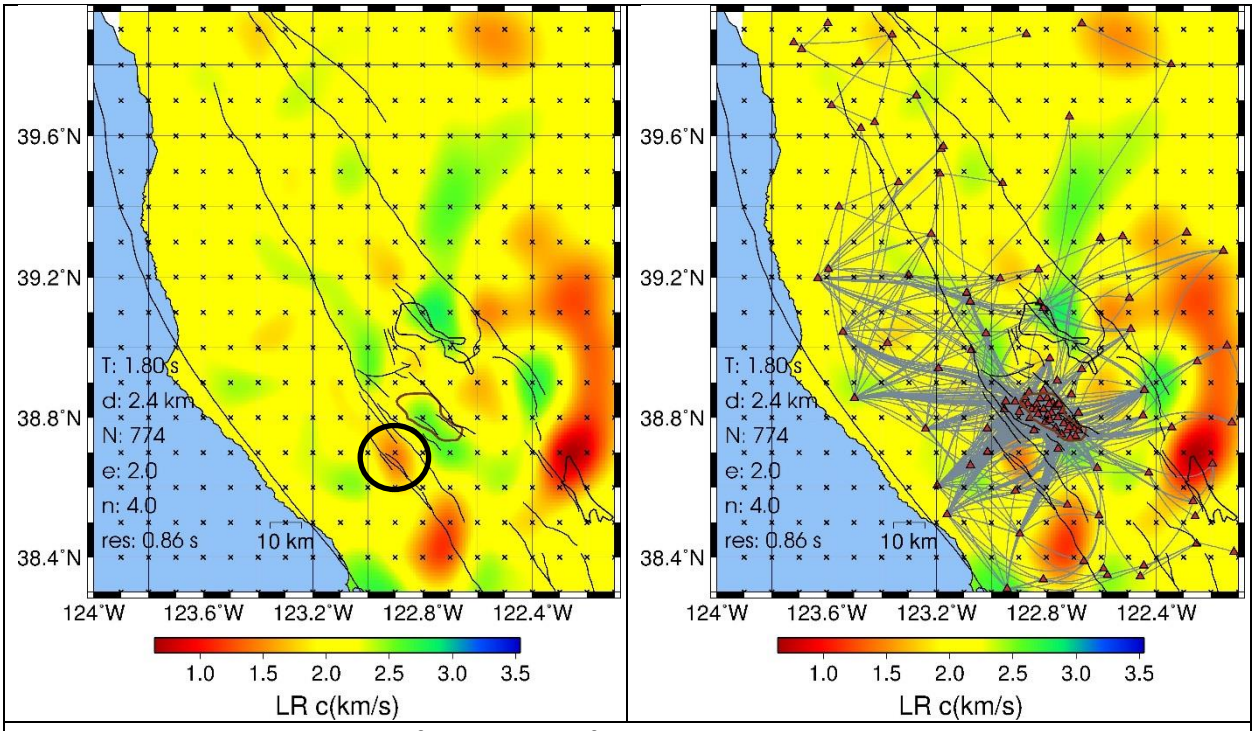

Figure 15: Same as Figure 14 for a period of T=1.80 s.

Figure 16 displays the phase velocity map of the period at T=1.99s, which has a maximum sensitivity at 2.7 km depth. With over 1,100 phase measurements the features in the vicinity of The Geysers and Clear Lake region are well resolved. Noted are the low velocity region below the Santa Rosa Valley, and the two low velocity anomalies, respectively located, between The Geysers and Clear Lake and to the southeast of Clear Lake. The latter two features seem to be connected to the shallow anomaly observed at the same locations in Figure 14. The velocity lows are consistent with results reported by Hearn et al. (1981), Eberhart-Phillips (1986) and Julian et al. (1996) and correlate to the region where the largest teleseismic station residuals were observed in Figure 5. Moreover, low velocity anomaly to the southeast of Clear Lake is consistent with the ambient noise-derived low Love wave phase velocities (2-5 s) between The Geysers and station MNRC reported by Nayak et al. (2017). Furthermore, the map in Figure 16 indicates that the shear wave velocities in The Geysers are higher than in the surrounding area as previously reported by Majer and McEvilly (1979) and Eberhart-Phillips (1986).

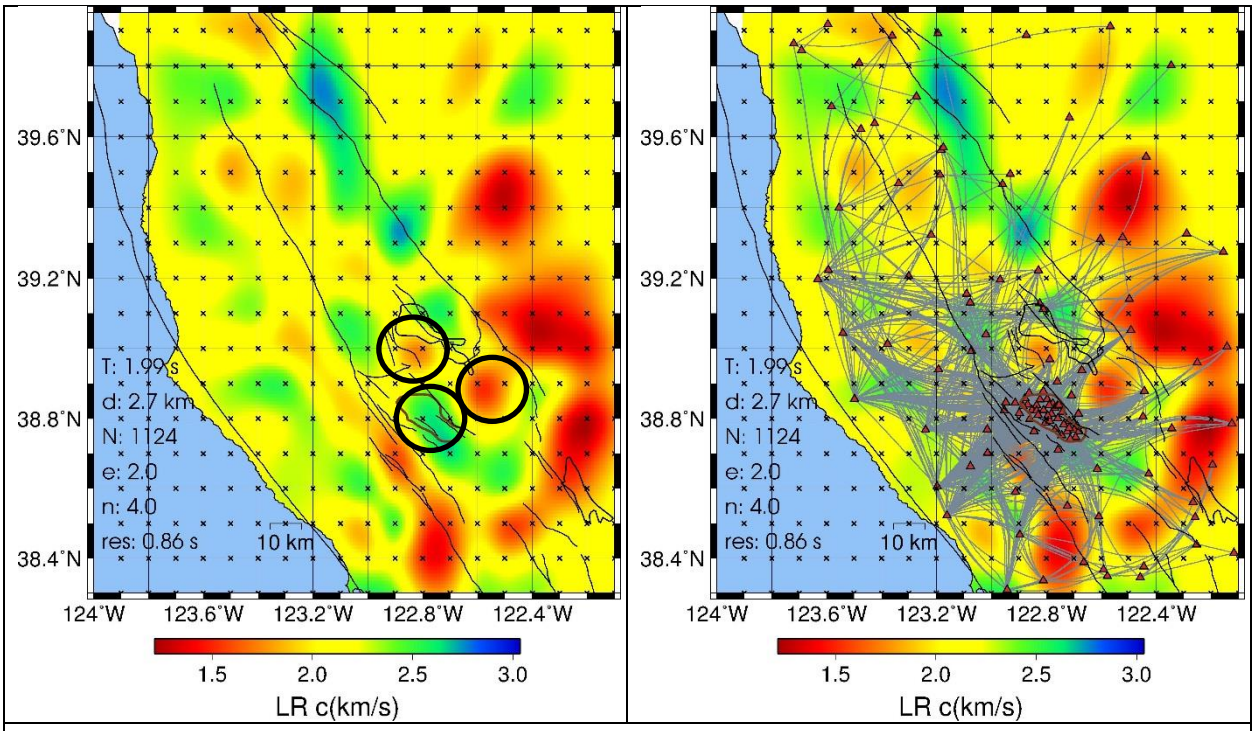

Figure 16: Same as Figure 14 for a period of T=1.99 s.

The phase velocity maps in Figures 17, 18, and 19 for periods of T=2.20s, T=2.44s, and T=2.7s, respectively, display the same features discussed thus far, for depth sensitivities between 3,0-3.8 km. The increase in the number of phase measurements with longer periods increases the resolution of the anomalies in each map. The two low-velocity anomalies, between The Geysers and Clear Lake and to the southeast of Clear Lake, decrease in amplitude with depth, while the latter one remains more prominent throughout these depth slices. The emergence of low velocity anomalies along the eastern margin of the study region indicates the presence of thick sediments in the northern central valley, which will be a persistent feature in the following phase velocity

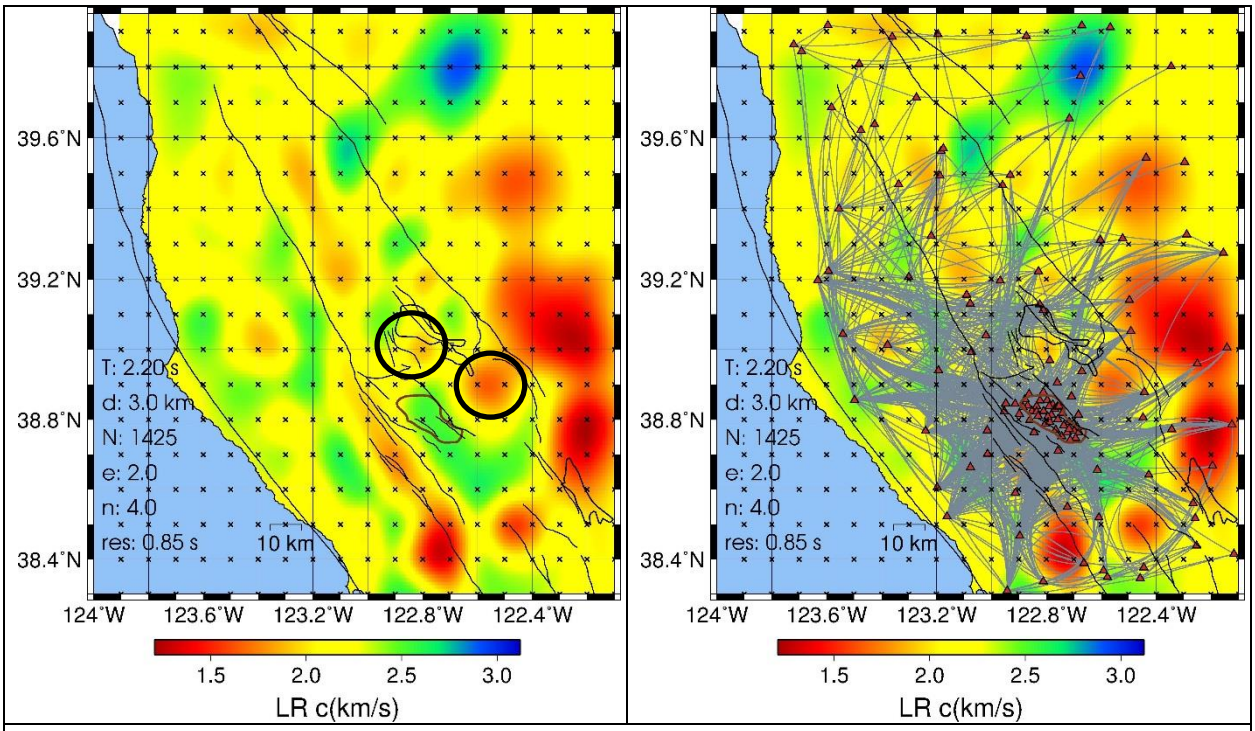

Figure 17: Same as Figure 14 for a period of T=2.20 s.

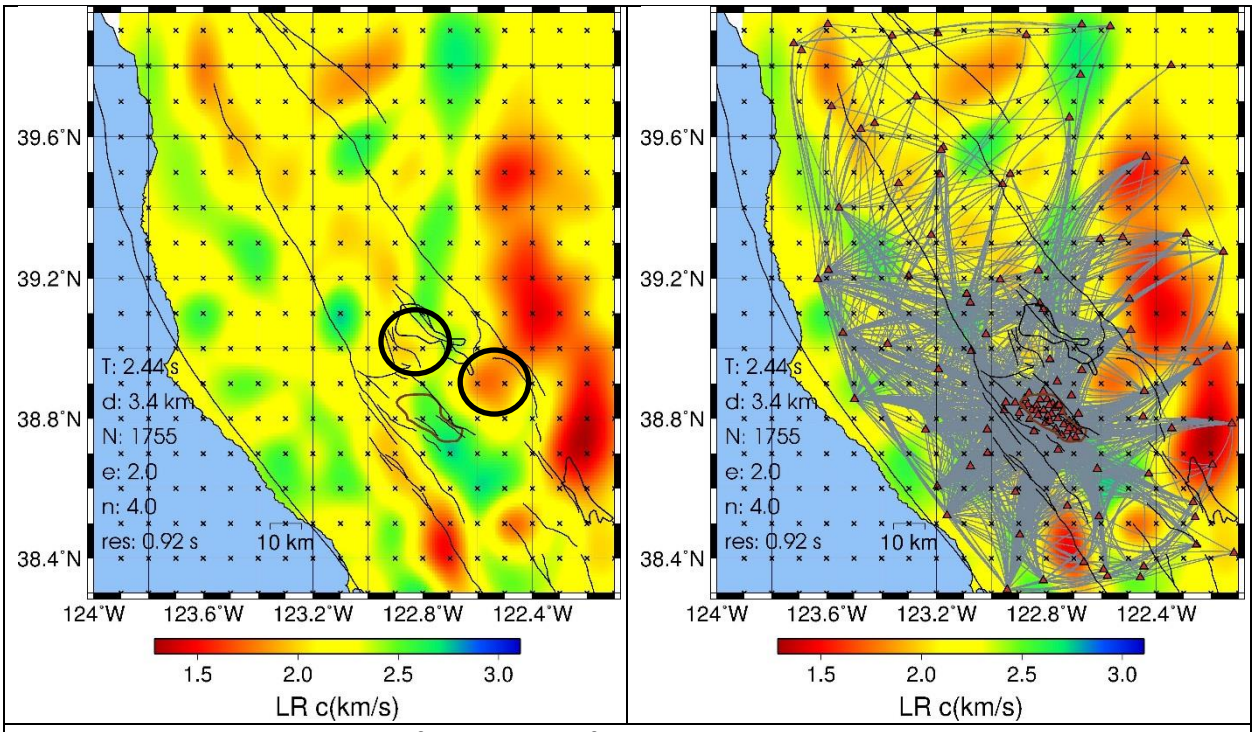

Figure 18: Same as Figure 14 for a period of T=2.44 s.

maps. These low velocities are consistent with the slow teleseismic travel-time residuals presented in Figure 4.

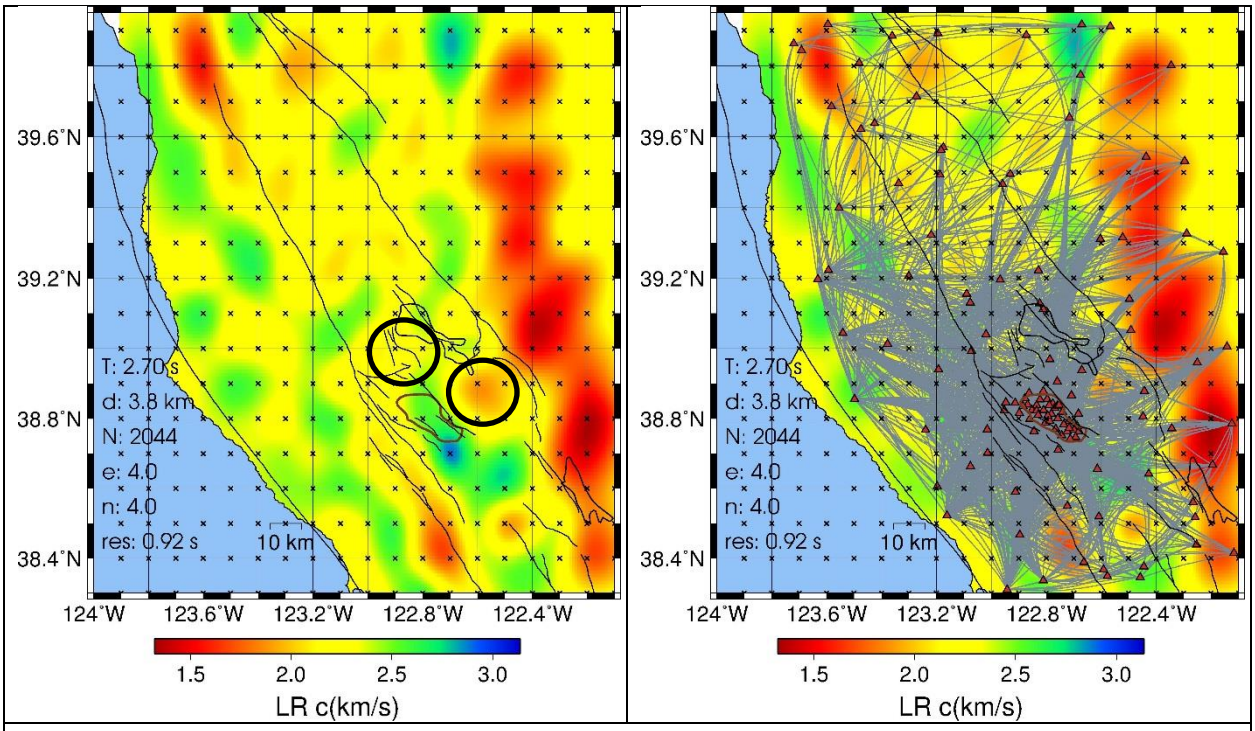

Figure 19: Same as Figure 14 for a period of T=2.70 s.

The next four Figures (20-23) represent phase velocity maps for periods ranging from T=2.98s to T=4.04s, which corresponds to a maximum depth sensitivity from 4.3 km to 6.1 km. A new emerging feature is the semi-linear low velocity zone trending parallel to the Bartlett Springs fault zone and extending into the northwest section of Clear Lake further south. The southern extension of this feature spatially correlates with the locations of the long-period events north of Clear Lake, as shown in Figure 7 (Section 2.3). At least on one phase velocity map (Figure 22) the low velocity feature reaches across Clear Lake and is visible below its northwestern shores, approximately where the second clusters of long-period events were located in Figure 7. To the south of The Geysers, a high velocity anomaly appears between the Mercuryville and Collayomi faults, which may be associated with igneous intrusives or high-grade metamorphism related to the underlying inferred partial-melt body (Eberhart-Phillips, 1986). This feature was already present in Figure 19 above. In Figure 23, the contrast in velocity estimates between the northwest and southeast Geysers becomes evident, with the northwest being slower than the southeast Geysers. This velocity contrast has also been reported in studies by Eberhart-Phillips (1986) Julian et al. (1996) and Gritto et al. (2013).

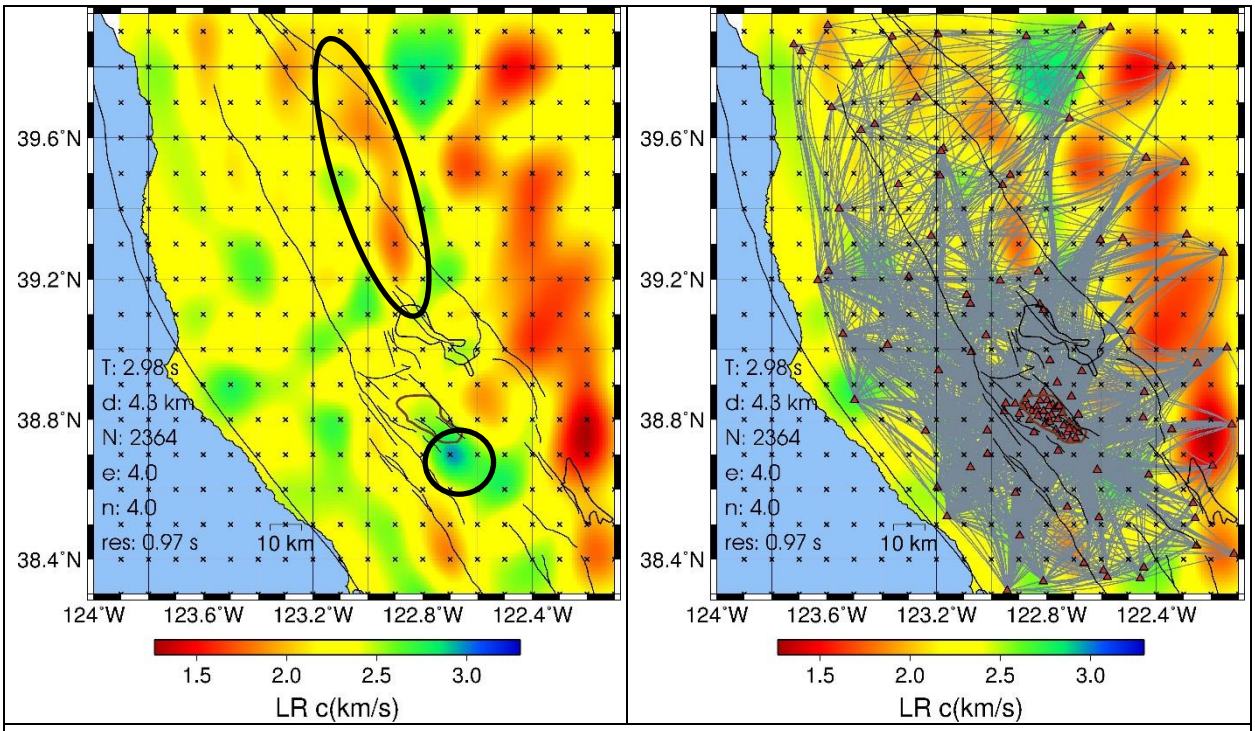

Figure 20: Same as Figure 14 for a period of T=2.98 s.

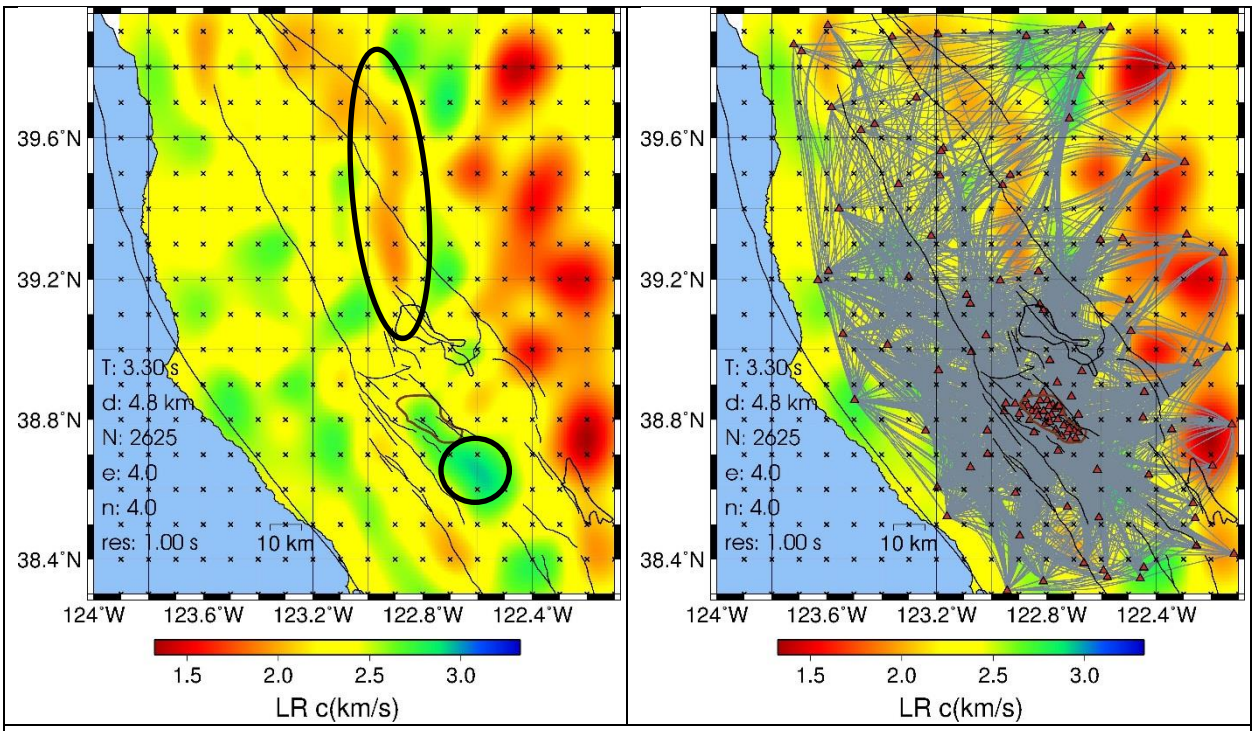

Figure 21: Same as Figure 14 for a period of T=3.30 s.

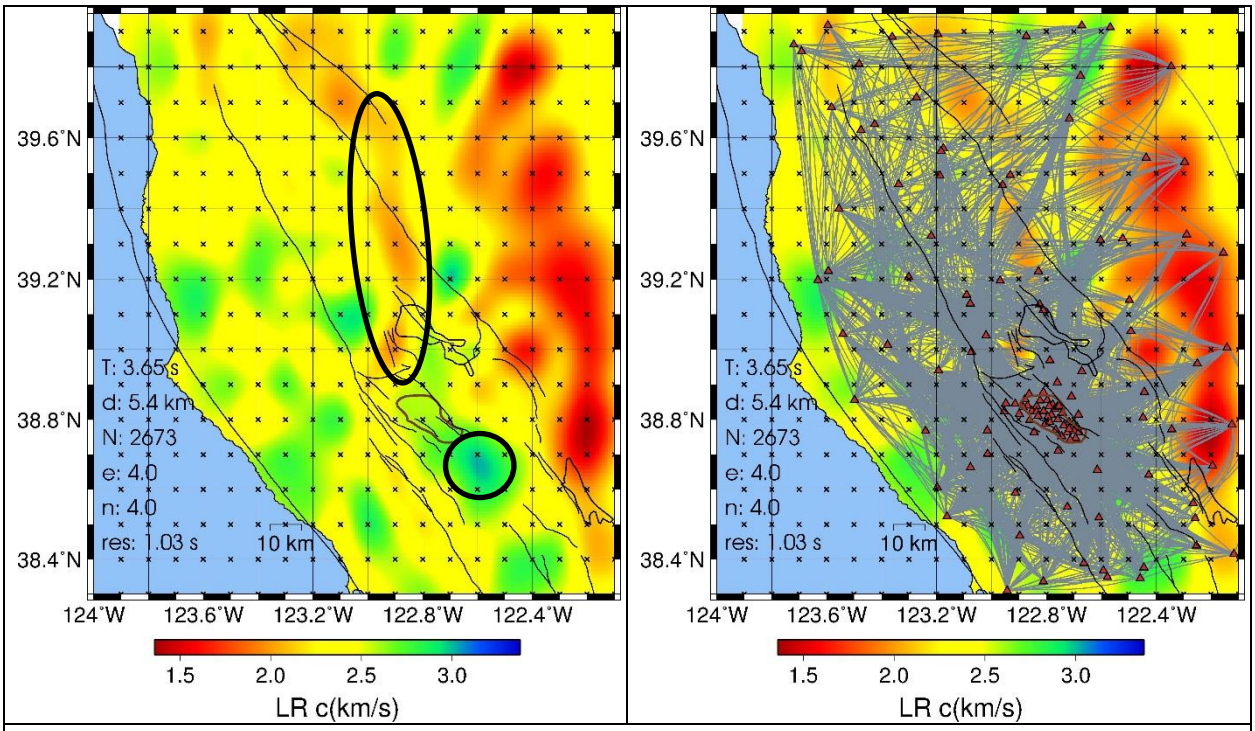

Figure 22: Same as Figure 14 for a period of T=3.65 s.

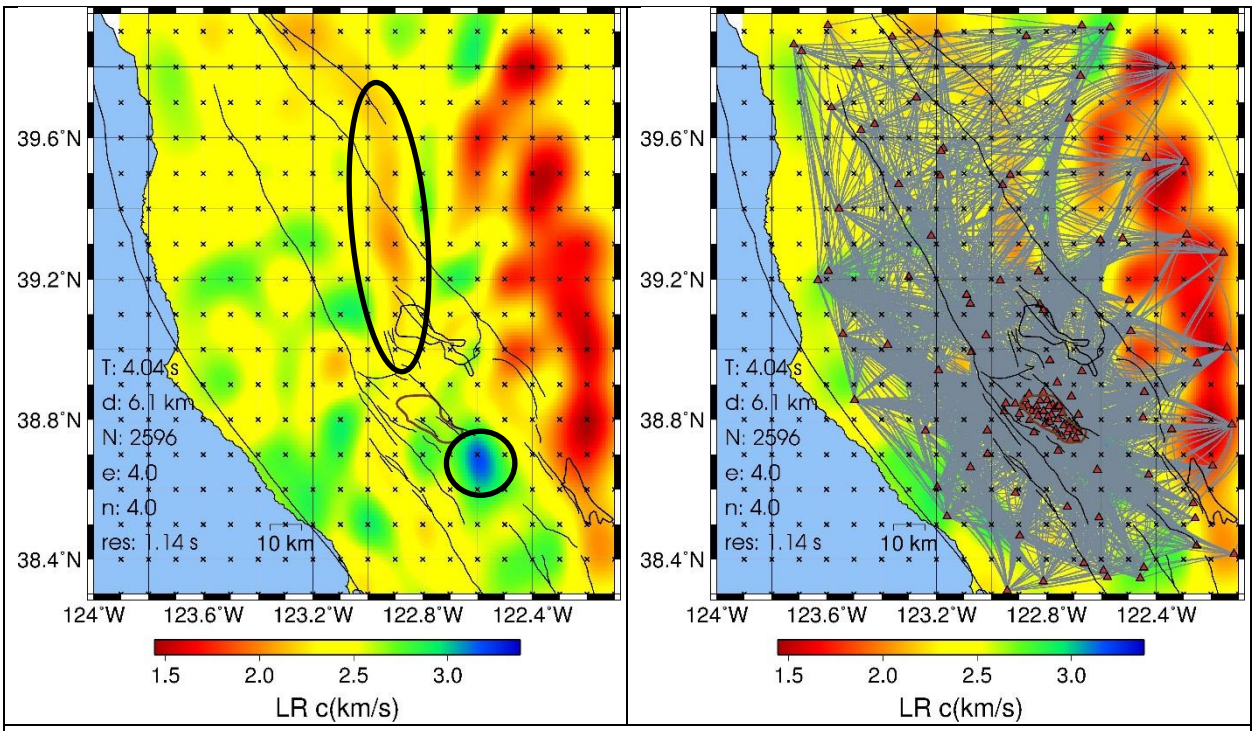

Figure 23: Same as Figure 14 for a period of T=4.04 s.

The low velocity anomaly trending north-south towards Clear Lake is still visible in Figure 24, which displays the phase velocity map for a period of T=4.46s and a maximum depth sensitivity of 6.9 km. At this depth, the velocity contrast across northwest-southeast axis of The Geysers is also visible. The reason that this velocity contrast only appears in the previous and current phase velocity maps, may be attributed to the node spacing of the inversion, which resulted in only one node covering The Geysers reservoir.

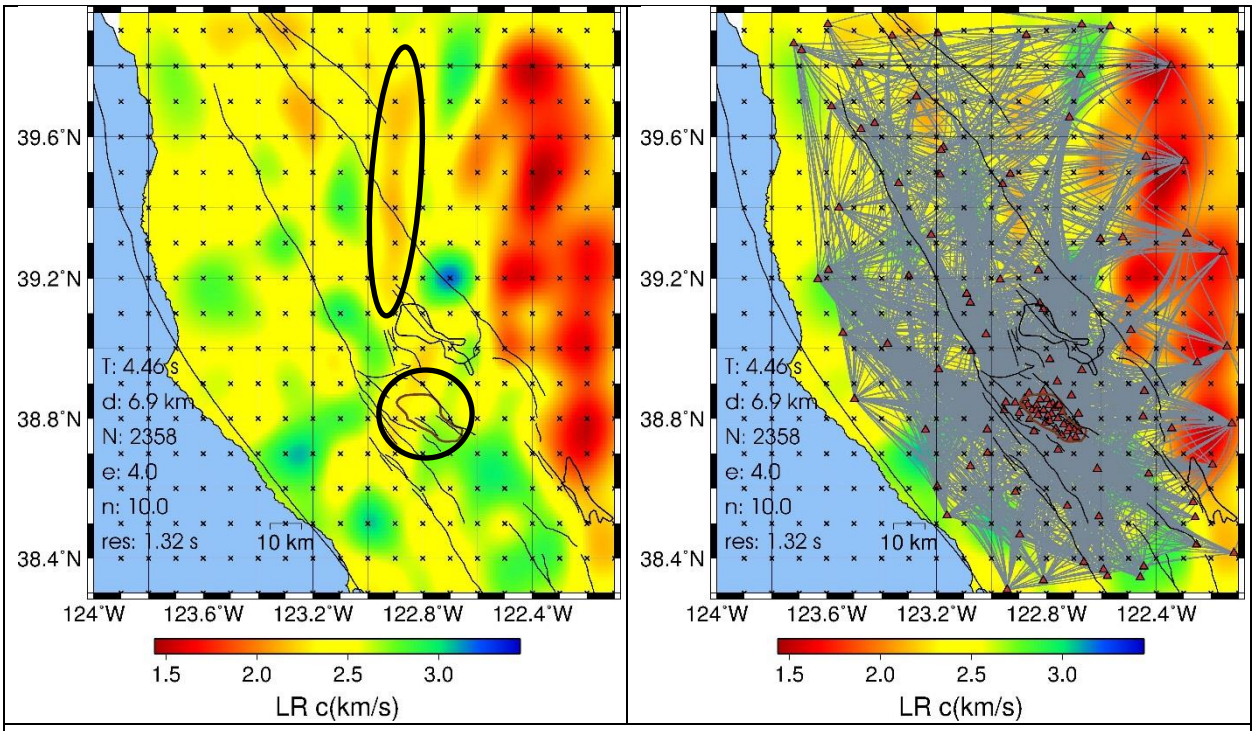

Figure 24: Same as Figure 14 for a period of T=4.46 s.

The results in the last three Figures (25 -27) may provide the most tantalizing evidence of a low velocity zone below The Geysers-Clear Lake volcanic complex. The figures present phase velocity maps for periods between T=4.94s and T=6.04s, with maximum depth sensitivities ranging from 7.7 km to 9.6 km. In each Figure, a well resolved low velocity anomaly can be seen north of The Geysers and southwest of Clear Lake. The location coincides with the cluster of tremors displayed in Figure 7. This feature is well resolved as documented by the high number of raypaths crossing this region. However, with the resolution provided by the current data, it is not possible to determine whether these low velocity anomalies are related to the shallower low velocity anomalies southwest and southeast of Clear Lake that were discussed in Figures 16-19. A joint temporary EM/seismic network may provide higher resolution data to address this question.

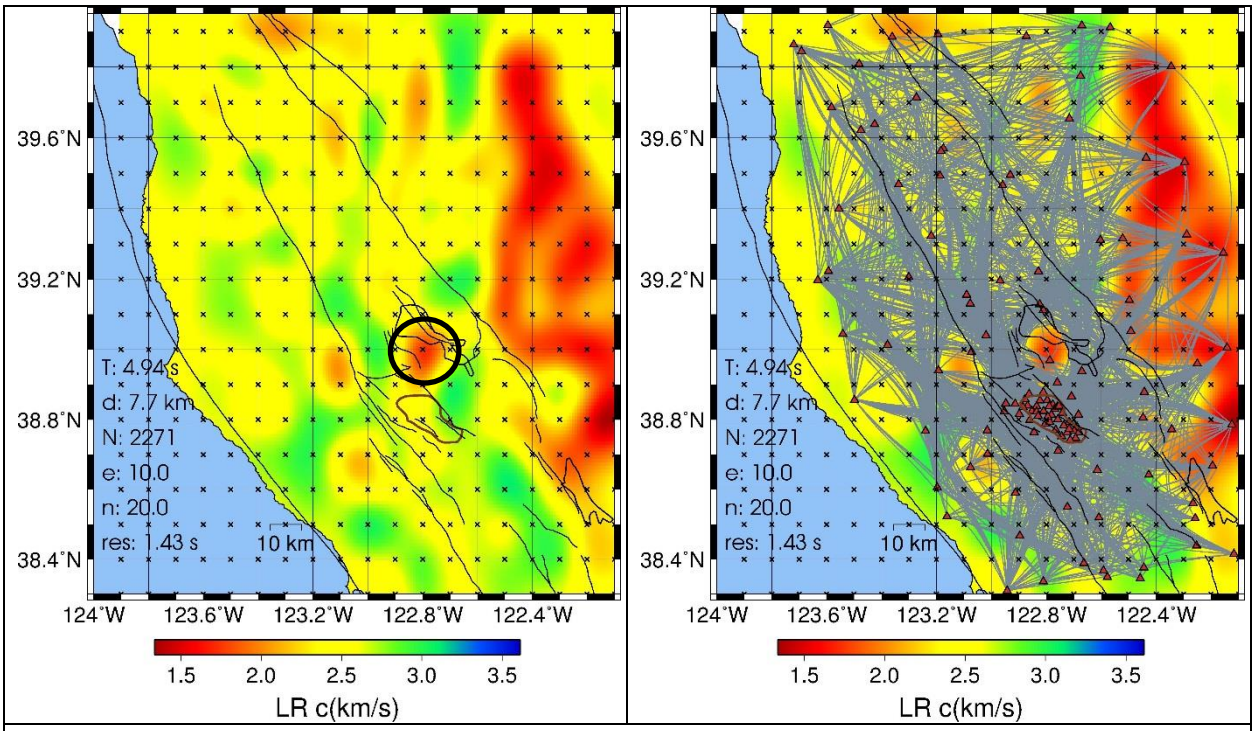

Figure 25: Same as Figure 14 for a period of T=4.94 s.

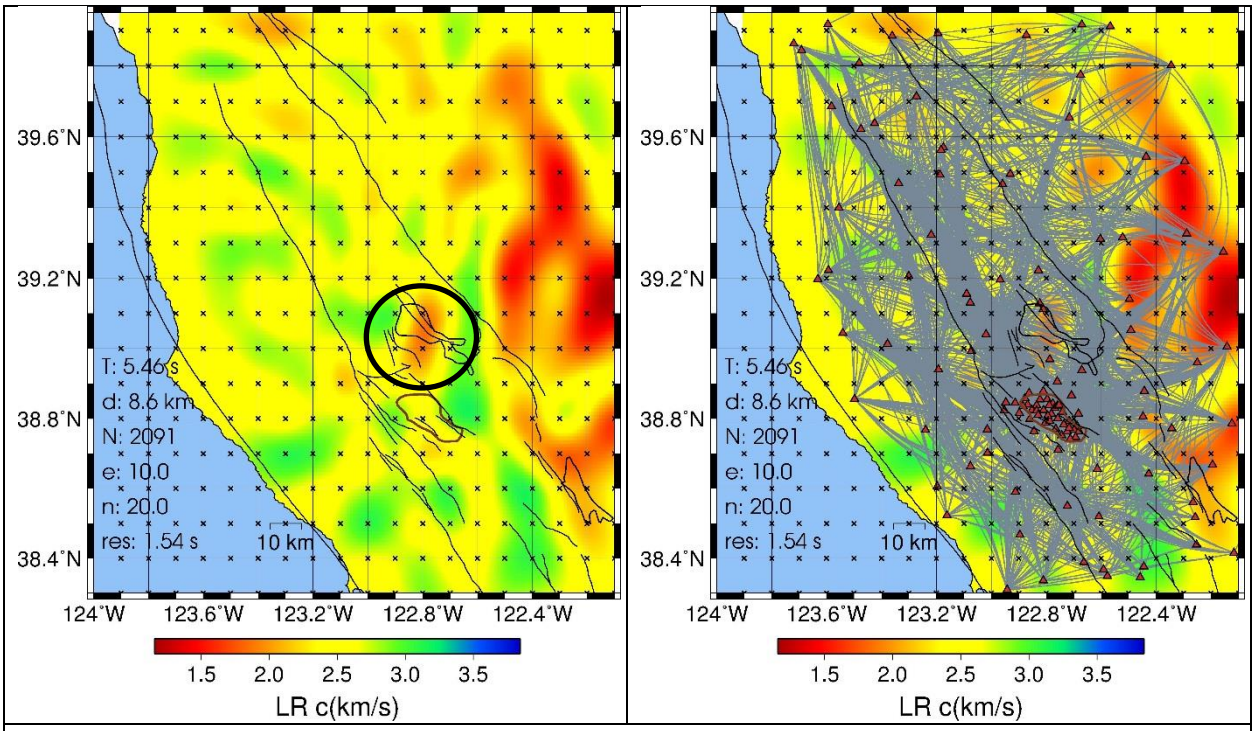

Figure 26: Same as Figure 14 for a period of T=5.46 s.

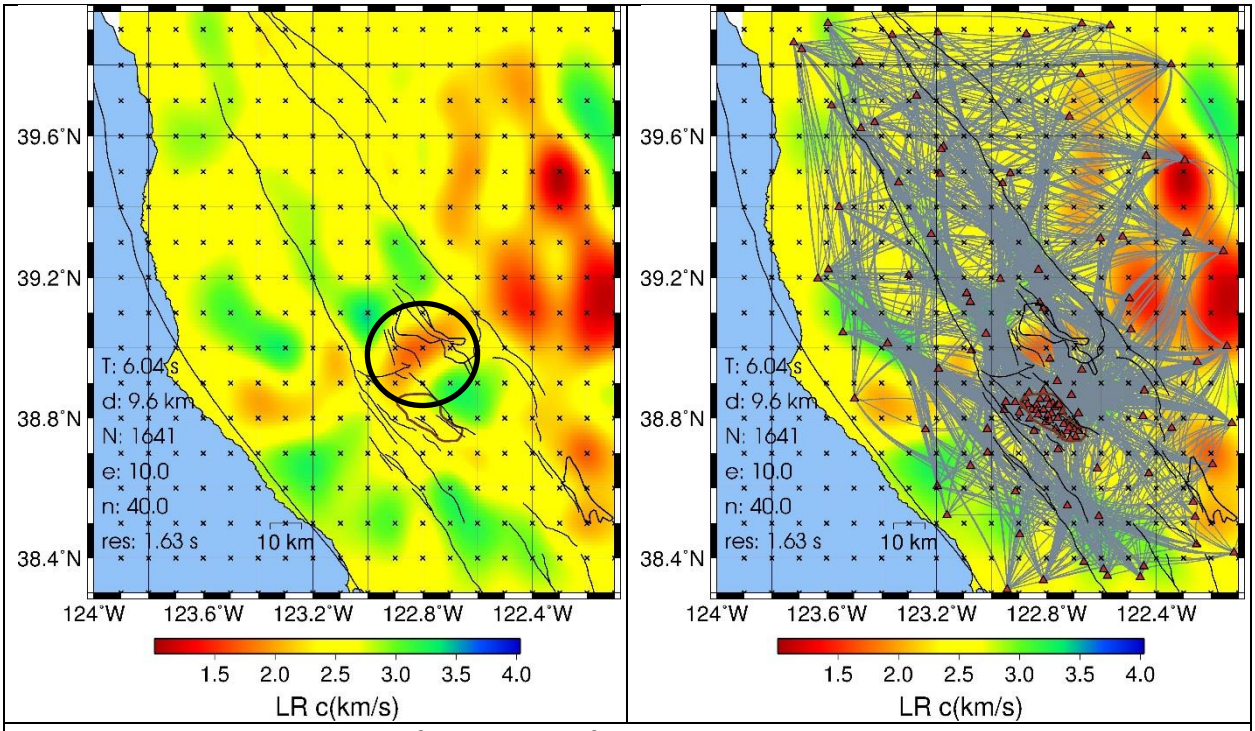

Figure 27: Same as Figure 14 for a period of T=6.04 s.

The above presented tomography results could be further refined based on the following suggestions.

(1) More sophisticated stacking methods such as phase-weighted stacking using the S-transform could improve the SNR of noise cross-correlations (Schimmel et al., 2011). RZ, ZR and ZZ component cross-correlations can be stacked after phase corrections to improve SNR of Rayleigh wave measurements.
(2) The phase velocity maps from the 1st round of the inversions could be used to construct new reference dispersion curves for re-measuring phase velocities on the noise cross-correlations. This step is expected to reduce the RMS residuals and add previously discarded outliers during the next round of inversions (e.g., Lin et al., 2008).
(3) The dense station spacing (~5-7 km) inside the reservoir area at The Geysers can be used for both, Love and Rayleigh wave Eikonal tomography (Lin et al., 2013) to study the velocity contrast between the northwest and the southeast Geysers (Julian et al., 1996; Gritto et al., 2013) at depths deeper than possible with body-wave tomography (> 3.5 km).

3 Recommendation for Future EM and Seismic Sensor Locations

Based on the results obtained in this study, the strongest evidence for crustal low-velocity structure that may be indicative of elevated temperatures was found through large negative travel time residuals for seismic stations located in the northwest Geysers geothermal reservoir and further northeast towards the southern part of Clear Lake, where the most recent volcanism of Mt. Konocti and Mt. Hana took place (Figure 28, left panel). The locations of these anomalies were supported by the interpretation of shear wave phase velocity maps derived from empirical Green Functions of ambient noise cross correlated data (Figure 29, right panel). Furthermore, a separate low velocity anomaly was observed at a depth of ~2-5 km to the southeast of Clear Lake (Figure 29, right panel). Additional evidence suggestive of fluid movement in the subsurface may be provided by the locations of long period earthquakes and tremors to the west and to the north of Clear Lake (Figure 28, right panel). These locations are also supported by the results of shear wave phase velocity maps that reveal low velocity anomalies at a depth of ~7-10 km. These anomalies are located between The Geysers and Clear Lake as well as to the northeast of Clear Lake (Figure 29).

Taking these results into consideration, potential sites for future deployment of EM and seismic sensors are marked by the black ellipses in Figures 28 and 29. These include the region north of The Geysers toward the southwestern shoreline of Clear Lake, the region north of Clear Lake, as well as a region to the southeast of Clear Lake. Logistical constraints should be considered, when planning data acquisition campaigns in this region. Figure 30 reveals a satellite map of Clear Lake including cities and roads. The main roads surrounding Clear Lake are Highways 20 and 29 located along the eastern and western shoreline, respectively. During any future EM or seismic survey, deployment sites should be locating away from these highways that connect cities around the lake. These cities include Upper Lake and Nice to the north, Lucerne and Clearlake Oaks to the east, Clear Lake and Lower Lake to the south, and Kelseyville, Lakeport and North Lakeport to the west. Because Highway 20 and 29 are located close to the shoreline and the cities are not too large, deployment of instruments in relatively quiet settings within 3-5 miles of the lake should be possible. The areas to the west and south of the lake have a lower topographic profile and are easier accessible than the areas to the east and north, which tend to be mountainous but offer a quieter setting compared to the southern and western shoreline.

However, if the goal of a potential seismic survey is the recording of ambient noise, the sensors may be deployed along Highways 20 and 29 to take advantage of urban traffic noise as a source to illuminate the subsurface. Similar experiments have been successfully conducted in the past, such as the Long Beach, CA experiment, where urban noise was utilized to image the fault structure of the region (Lin et al, 2013; Nakata et al., 2015). It is noted, however, that seismic sensors deployed along Highways 20 and 29, may not be able to detect the small-magnitude events that occur in this region. Therefore, a combination of sensors in more quiet settings at greater distances from the lake and along the highways around Clear Lake may offer the best combination to take advantage of the natural seismicity and ambient noise characteristics.

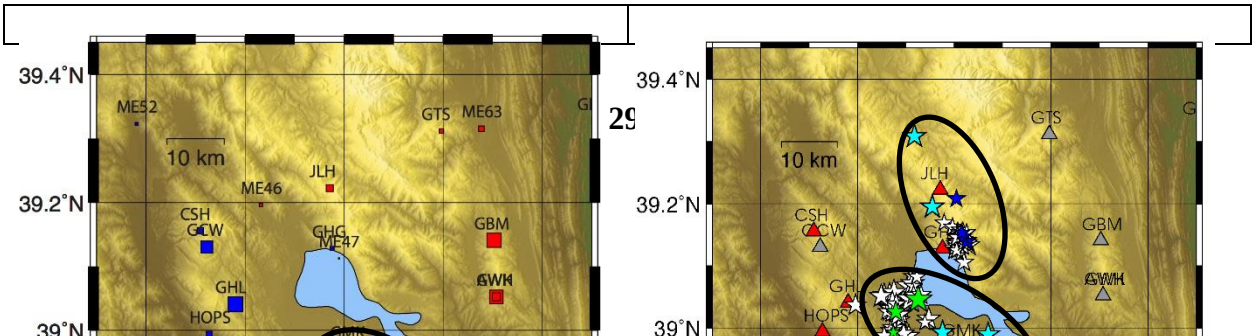

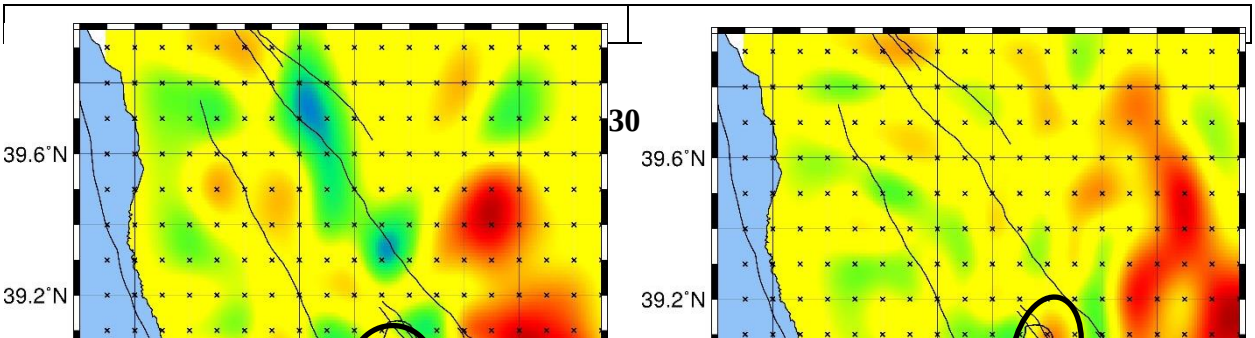

Figure 28: Maps of teleseismic travel time residuals (left) and locations of LP and tremor events (right) with recommended sites for future deployment of EM and seismic sensors (black ellipses).

Figure 29: Maps of Rayleigh wave phase velocities with recommended sites for future deployment of EM and seismic sensors (black ellipses).

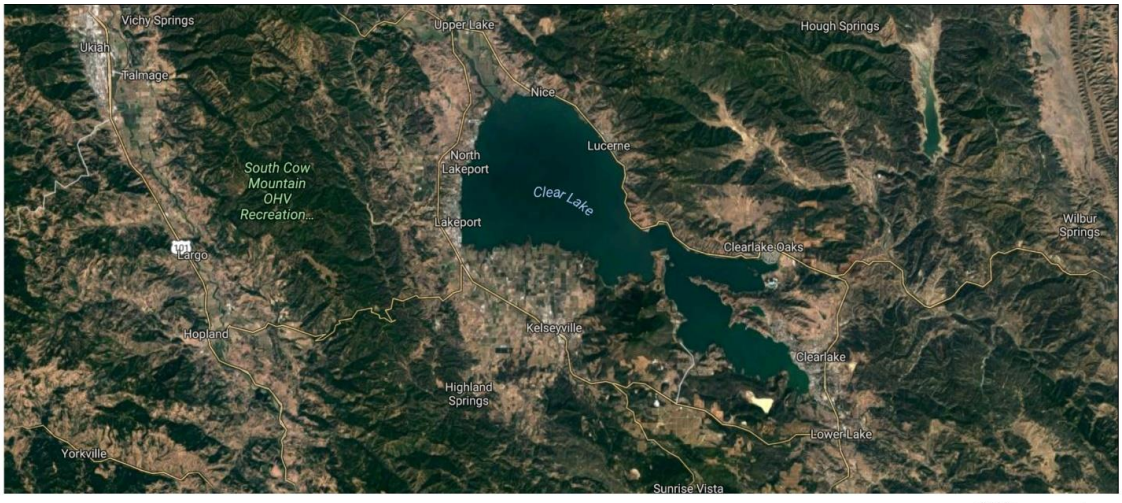

Figure 30: Map of Clear Lake and its surrounding areas.

4 Acknowledgments

Seismic data from the Berkeley Digital Seismic Network (BDSN, network code BK), Lawrence Berkeley National Laboratory (LBNL, BG), and the Northern California Seismic Network (NCSN, NC) were provided by the Northern California Earthquake Data Center (NCEDC), Berkeley Seismological Laboratory, University of California, Berkeley, and U.S. Geological Survey, Menlo Park. Data were also acquired from the EarthScope Transportable Array (TA), Mendocino Experiment (FAME)- EarthScope Flex Array (XQ), and the Plate Boundary Observatory Borehole Seismic Network (PB), all archived at the Incorporated Research Institutions in Seismology (IRIS) Data Management Center.

5 References

Aagaard, B.T., R.W. Graves, A. Rodgers, T.M. Brocher, R.W. Simpson, D.S Dreger, N.A. Petersson, S.C. Larsen, S. Ma, and R.C. Jachens (2010). Ground-motion modeling of Hayward fault scenario earthquakes, part II: Simulation of long-period and broadband ground motions, Bull. Seismol. Soc. Am. 100(6) 2945–2977, doi: 10.1785/0120090379.

Aguiar, A.C., T.I. Melbourne, Scrivner, C.W. (2009). Moment release rate of Cascadia tremor constrained by GPS. J. Geophys. Res., 114, B00A05, doi:10.1029/2008JB005909.

Barmin, M.P., M.H. Ritzwoller & A.L. Levshin (2001). A fast and reliable method for surface wave tomography, Pure. Appl. Geophys. 158, 1351-1375.

Bensen, G.D., Ritzwoller, M.H., Barmin, M.P., Levshin, A.L., Lin, F.-C., Moschetti, M.P., Shapiro, N.M. & Yang, Y. (2007). Processing seismic ambient noise data to obtain reliable broadband surface wave dispersion measurements, Geophys. J. Int., 169, 1239–1260, doi: 10.1111/j.1365-246X.2007.03374.x.

Benz, H.M., G. Zandt and D.H. Oppenheimer (1992). Lithospheric Structure of Northern California From Teleseismic Images of the Upper Mantle, J. Geophys. Res. 97(B4), 4791-4807.

Brocher, T. (2008). Compressional and shear-wave velocity versus depth relations for common rock types in northern California, Bull. Seismol. Soc. Am. 98, 2, 950–968, doi 10.1785/0120060403.

Chouet, B. (1992). A seismic model for the source of long-period events and harmonic tremor, Volcanic Seismology, Vol. 3., 133-156.

Chouet, B. (1996). New methods and future trends in seismological volcano monitoring, in R. Scarpa and R. I. Tilling (editors). Monitoring and Mitigation of Volcano Hazards, Berlin, Heidelberg, Springer-Verlag, 23-97. Chouet, B.A., P.B. Dawson, and M. Martini (2008). Shallow-conduit dynamics at Stromboli Volcano, Italy, imaged from waveform inversions, Geol. Soc. London Spl. Pub., 307, 57-84, doi: 10.1144/SP307.5.

Eberhart-Phillips, D. & Oppenheimer, D.H., 1984. Induced seismicity in The Geysers geothermal area, California, J. Geophys. Res., 82(B2), 1191-1207.

Eberhart-Phillips, D., 1986. Three-dimensional velocity structure in northern California Coast Ranges from inversion of local earthquake arrival times, Bull. Seismol. Soc. Am., 76(4), 1025-1052.

Guilhem, A., Z. Peng and R.M. Nadeau (2010). High-frequency identification of non-volcanic tremor triggered by regional earthquakes, Geophys. Res. Lett., 37, L16309, doi:10.1029/2010GL044660, 2010.

Gritto, R., S.-H. Yoo, and S.P. Jarpe (2013). 3D seismic tomography at The Geysers geothermal field, CA, USA, in proceedings of Thirty-Eighth Workshop on Geothermal Reservoir Engineering, Stanford University, California, 11-13 February 2013.

Hearn, Jr., B.C., Donnelly-Nolan, J.M. & Goff, F.E., 1981. The Clear Lake volcanics: Tectonic setting and magma sources, U.S. Geol. Surv. Prof. Pap. 1141, 25-45.

Herrmann, R.B. (2013). Computer programs in seismology: An evolving tool for instruction and research, Seism. Res. Lett. 84, 1081-1088, doi:10.1785/0220110096.

Julian, B.R. (1994). Volcanic tremor: non-linear excitation by fluid flow, J. Geophys. Res. 99, B6, 11859-11877.

Julian, B.R., Ross, A., Foulger, G.R. & Evans, J.R., 1996. Three-dimensional seismic image of a geothermal reservoir: The Geysers, California, Geophys. Res. Lett., 23(6), 685-688.

Kennett B.L.N., Engdahl E.R. and Buland R. (1995). Constraints on seismic velocities in the earth from travel times, Geophys. J. Int. 122, 108-124.

Lin, F.-C., M.P. Moschetti, and M.H. Ritzwoller (2008). Surface wave tomography of the western United States from ambient seismic noise: Rayleigh and Love wave phase velocity maps, Geophys. J. Int. 173, 281-298, doi: 10.1111/j.1365- 246X.2008.03720.x.

Lin, F.-C., D. Li, R.W. Clayton, and D. Hollis (2013). High-resolution 3D shallow crustal structure in Long Beach, California: Application of ambient noise tomography on a dense seismic array, Geophys. 78(4), Q45–Q56, doi: 10.1190/GEO2012-0453.1

Lin, F.-C., V.C. Tsai and B. Schmandt (2014). 3-D crustal structure of the western United States: application of Rayleigh-wave ellipticity extracted from noise cross-correlations, Geophys. J. Int. 198, 656-670, doi: 10.1093/gji/ggu160.

Lou, X., S. van der Lee and S. Llyod (2013). AIMBAT: A Python/Matplotlib tool for measuring teleseismic arrival times, Seism. Res. Lett. 84(1), 85-93, doi: 10.1785/0220120033.

Majer, E.L., and T.V. McEvilly (1979). Seismological investigations at The Geysers geothermal field, Geophys., 44, 2, 246-269.

Nadeau, R.M. and A. Guilhem (2009), Nonvolcanic tremor evolution and the San Simeon and Parkfield, California earthquakes, Science, 325, 191-193, doi:10.1126/science.1174155.

Nakata, N., J. Chang, J.F. Lawrence and P. Boué, 2015. Body wave extraction and tomography at Long Beach, California, using ambient noise interferometery, J. Geophys. Res., 120, 1159-1173, doi: 10.1002/2015JB011870.

Nayak, A., T. Taira, D.S. Dreger and R. Gritto (2017). Empirical Green's tensor derived from ambient noise cross-correlations at The Geysers geothermal field, northern California, under revision in Geophys. J. Int.

Oppenheimer, D.H. and K.E. Herkenhoff (1981). Velocity-density properties of the lithosphere from three-dimensional modeling at The Geysers-Clear Lake region, California, J. Geophys. Res. 86, 6057-6065.

Pitt, A.M., D.P. Hill, S.W. Walter, and M.J.S. Johnson (2002). Midcrustal, long-period earthquakes beneath northern California volcanic areas, Seis. Res. Lett. 73(2), 144-152.

Porritt, R.W., R.M. Allen, D.C. Boyarko & M.R. Brudzinski (2011). Investigation of Cascadia segmentation with ambient noise tomography, Earth Planet. Sci. Lett. 309, 67–76, doi:10.1016/j.epsl.2011.06.026.

Rawlinson, N. and M. Sambridge (2003). Seismic traveltime tomography of the crust and lithosphere, Advances in Geophysics 46, 81-198.

Rawlinson, N. and M. Sambridge (2004). Wavefront evolution in strongly het- erogeneous layered media using the fast marching method, Geophys. J. Int. 156, 631-647.

Rawlinson, N. (2008). FMST: Fast Marching Surface Tomography Package v. 1.1 – Instructions.

Rogers, G., and H. Dragert (2003), Episodic tremor and slip on the Cascadia subduction zone: The chatter of silent slip, Science, 300, 1942-1943.

Schwartz, S. Y., and J. M. Rokosky (2007), Slow slip events and seismic tremor at circum-Pacific subduction zones, Rev. Geophys., 45, RG3004, doi:10.1029/2006RG000208.

Schimmel, M., E. Stutzmann, and J. Gallart (2011). Using instantaneous phase coherence for signal extract from ambient noise data at a local to a global scale, Geophys. J. Int. 184, 494–506 doi: 10.1111/j.1365-246X.2010.04861.x

Seats, K.J., J.F. Lawrence, and G.A. Prieto (2012). Improved ambient noise correlation functions using Welch's method, Geophys. J. Int., 188, 513–523, doi: 10.1111/j.1365-246X.2011.05263.x.

Sens-Schönfelder, C. (2008). Synchronizing seismic networks with ambient noise, Geophys. J. Int., 174, 966–970, doi: 10.1111/j.1365-246X.2008.03842.x.

Shelly, D. R., G. C. Beroza, S. Ide, and S. Nakamura, (2006). Low-frequency earthquakes in Shikoku, Japan and their relationship to episodic tremor and slip, Nature, 442, 188-191, doi:10.1038/nature04931.

Spica Z., M. Perton, M. Calo, D. Legrand, F. Cordoba-Montiel, and A. Iglesias (2016), 3-D shear wave velocity model of Mexico and South US: bridging seismic networks with ambient noise cross-correlations and correlation of coda of correlations, Geophys. J. Int., 206, 1795-1813, doi: 0.1093/gji/ggw240

Song, T.-R., D.V. Helmberger, M.R. Brudzinski, R.W. Clayton, P. Davis, X. Perez-Campos, S.K. Singh, (2009), Subducting slab ultra-slow velocity layer coincident with silent earthquakes in southern Mexico, Science, 324, 502–505, doi:10.1126/science.1167595.

Stanley, W.D., H.M. Benz, M.A. Walters, A. Villasenor, and B.D. Rodriguez (1998). Tectonic controls on magmatism in The Geysers-Clear Lake region: Evidence from new geophysical models, Geol. Soc. Am. Bull., 110, 1193– 1207.

Stehly, L., M. Campillo, B. Froment, and R.L. Weaver (2008). Reconstructing Green's function by correlation of the coda of the correlation (C^3) of ambient seismic noise, J. Geophys. Res. 113, B11306, doi:10.1029/2008JB005693.

Stidham, C., M. Antolik, D.S. Dreger, S. Larsen and B. Romanowicz (1999). Three-dimensional structure influences on the strong motion wavefield of the 1989 Loma Prieta earthquake, Bull. Seism. Soc. Am., 89, 1184-1202.

Thomas, A. M., R. M. Nadeau, and R. Bürgmann (2009), Tremor-tide correlations and near-lithostatic pore pressure on the deep San Andreas fault, Nature, 462, 1048-1051, doi:10.1038/nature08654.

Thomas, A. M., G.C.Beroza, and D.R. Shelly (2016), Constraints on the source parameters of low-frequency earthquakes on the San Andreas Fault, Geophys. Res. Lett., 43, doi:10.1002/2015GL067173.

Thurber, C., H. Zhang, T. Brocher and V. Langenheim (2009). Regional three-dimensional seismic velocity model of the crust and uppermost mantle of northern California, J. Geophys. Res. 114, B01304, doi:10.1029/2008JB005766.

VanDecar, J.C. and R.S. Crosson (1990). Determination of teleseismic relative phase arrival time using multi-channel cross-correlation and least squares, Bull. Seism. Soc. Am. 80(1), 150-169.

Xia, J., R.D. Miller, and C.B. Park, 1999. Estimation of near-surface shear- wave velocity by inversion of Rayleigh waves, Geophys., 64, 691–700, doi: 10.1190/1.1444578.